KTH Engineering Sciences

Experimental and numerical study of a high-repetition rate Yb-fiber amplifier source

by
Robert Lindberg
Supervisor
Valdas Pasiskevicius
Examinator
Fredrik Laurell

Master of Science Thesis

Laser Physics
Department of Applied Physics
School of Engineering Science
Royal Institute of Technology

Stockholm, Sweden 2014

TRITA-FYS 2014:12
ISSN 0280-316X
ISRN KTH/FYS/--14:12--SE

Abstract

An Ytterbium doped optical fiber was used as an amplifier in a master oscillator power amplifier setup, where the master oscillator was a high repetition rate mode-locked 170 fs laser. The effect of the amplifier was quantified by measuring the power, spectrum and pulse duration of the output for an average input power of 0.36 W with varied pump power. This amplifier setup had a slope efficiency of 76% and yielded 3 ps pulses with an average power of 9.7 W at the maximum applied pump power, 16 W.

A numerical study of the amplifier was also conducted by developing a model combining the generalized nonlinear Schrödinger equation and the steady state rate equations. This was done in order to account for a non constant gain as well as nonlinear effects, as opposed to the general case, when studying pulse propagation in fibers, of approximating the gain to be constant and only using the generalized nonlinear Schrödinger equation. Furthermore, a series expansion accounting for gain dispersion was also included in the generalized nonlinear Schrödinger equation. In all, the combined model accounts for the effects of group velocity dispersion, self phase modulation, self-steepening, the Raman effect, gain dispersion and non constant gain. The model predicts an amplifier with a slope efficiency of 77 % yielding 2.8 ps pulses with an average power of 9.6 W for an applied pump power of 16 W.

Acknowledgements

I would first and foremost like to extend my gratitude and appreciation to my two informal supervisors, Dr. Mikael Malmström and PhD Peter Zeil, for their support and assistance throughout this work. An additional special thanks to PhD Peter Zeil for all the enlightening and insightful discussions regarding the simulations and also for all the time he spent helping me out with the experimental setup.

Furthermore I would like to thank Prof. Valdas Pasiskevicius for an interesting and inspiring course in laser physics that got me interested in the field. Another thanks to him and also to Prof. Fredrik Laurell for letting me do my master thesis at the laser physics division at Kungliga Tekniska Högskolan.

I would also like to thank the rest of the laser physics group for making me feel welcome. Another big thanks to my fellow master students, also doing their theses at the laser physics division, Robert Hurra and Pavel Delgado, for lighetning up my time there.

Lastly, I want to thank my family and my friends for their support during my time at Kungliga Tekniska Högskolan.

Contents

List of Figures

List of Tables

Acronyms

ASE Amplified Spontaneous Emission

FWHM Full Width Half Maximum

GVD Group Velocity Dispersion

GNLS Generalized Nonlinear Schrödinger Equation

HR High reflective

HT High transmitting

MOPA Master Oscillator Power Amplifier

NA Numerical Aperture

NLS Nonlinear Schrödinger Equation

RK4 Fourth-Order Runge-Kutta method

RK4IP Fourth-Order Runge-Kutta In The Interaction Picture method

SE Spontaneous Emission

SPM Self Phase Modulation

SVEA Slowly Varying Envelope Approximation

TIR Total Internal Reflection

Yb Ytterbium

1 Introduction

A short background to this master thesis, its aim and outline are given below.

1.1 Background

Today pulsed lasers are used in numerous applications ranging from telecoms and the study of chemical processes to cutting, welding and drilling. The laser beams used in high power applications, such as laser cutting, are often achieved by master oscillator power amplifier, MOPA, setups. The master oscillator provides a laser beam with desired characteristics and seeds the amplifier stage which scales the seed to the necessary power levels.

The power amplifier can be realized by letting the master oscillator output pass through a pumped active medium multiple times, either in a multipass or regenerative scheme. The multipass scheme uses mirrors to let the master oscillator output pass through the active medium multiple times from different directions, usually making the alignment very cumbersome. In a regenerative amplifier the active medium is placed in a cavity, which in general makes it easier to align, and a shutter is used to control the number of passes. However, the gain is strongly affected by intra-cavity losses. It has also been shown that for high repetition rates of the master oscillator pulses, the output power of a regenerative amplifier can fluctuate [2].

A more easily aligned rapidly growing contender to the above mentioned amplifier schemes is the fiber amplifier. A fiber amplifier consists of rare-earth ions doped into a glass matrix. The amorphous structure of glass makes the doped ions experience different local electric fields which in turn give different Stark splitting. This effect and the interaction between dopants and glass phonons broaden the energy levels resulting in a broad gain bandwidth, thus making fiber amplifiers suitable for ultra-short pulse amplification. The rare-earth ions store energy which is then given to the master oscillator output. Yt-terbium, Yb, ions have pumping schemes with low quantum defect and are currently the rare-earth ions with the best power scaling [3]. Hence, Yb-ions are commonly used in high power applications. Yb-doped fibers also provide a broad gain bandwidth extending from 970 to 1200 nm as well as a broad absorption band from 800 to 1064 nm [1]. The pump window thus cover the wavelengths at which high power laser diodes perform best [3].

The cylindrical form of a fiber gives a large surface to volume ratio which results in better heat dissipation than in bulk solid-state active medium [4], which is extremely important in high power applications. However, fiber amplifiers also have disadvantages compared to multipass and regenerative amplifiers:

- Due to long propagation distance, dispersive and nonlinear effects, such as group velocity dispersion and self phase modulation, become more pronounced in fiber amplifiers, than in the active medium used in regenerative and multipass amplifiers. This can make it more difficult to achieve high peak powers.
- The high gain in fiber amplifiers makes them sensitive to back reflections, from the fiber's end faces or other elements in the amplifier setup, which can lead to parasitic lasing.
- As the fiber is a closed system it is only possible to measure the in- and output while it is possible to probe the beam in multipass and regenerative amplifiers. This

makes modeling fiber amplifiers more difficult as the intermediate stages cannot be used to check the model's validity.

1.2 Purpose of this master thesis

Much of the modeling of fiber amplifiers have been done only using a rate equations approach, which accounts for a non constant gain, see for example [5, 6, 7, 8]. The problem with the rate equations approach is that it does not account for important nonlinear effects, which should be taken into account when modeling pulse amplification. Another common approach is to consider the fiber gain to be constant and only using the propagation equation for optical pulses in fibers, the generalized nonlinear Schrödinger equation. The purpose of this master thesis is to combine the rate equations with the generalized nonlinear Schrödinger equation. The combined generalized model is to be solved numerically in MATLAB. Validation of the model will consist of setting up and modeling a MOPA setup and compare the simulated results to experimentally collected data.

1.3 Thesis outline

The basic principles on which optical fibers are based are given in section 2. The generalized nonlinear Schrödinger equation and the rate equations are introduced and described in section 3. Section 4 outlines how the models are combined and solved numerically. In section 5 the setting of the simulation parameters is detailed. The experimental setup is explained in section 6. In section 7, the results are presented. Section 8 discusses the results and the model. A summary of the thesis, conclusions and future work are given in section 9.

2 Fiber basics

The main task of an optical fiber is to guide incident light from one end to the other. This is achieved by a phenomenon called total internal reflection, TIR. TIR can be understood by the use of Snell's law

$$n_1 \sin\theta_1 = n_2 \sin\theta_2 \tag{1}$$

where n_1 and n_2 are the refractive indexes of two different regions and θ_1 and θ_2 are the incident and refracted angels of light with respect to the surface normal, see Figure 1. It follows from Snell's law that if $n_1 > n_2$ then $\theta_1 < \theta_2$. In this case, there is a critical incidence angle $\theta_1 = \theta_c$ at which $\theta_2 = 90°$.

$$n_1 \sin\theta_c = n_2 \sin(90°) \Rightarrow \theta_c = \arcsin\frac{n_2}{n_1} \tag{2}$$

This means that for $\theta_1 \geq \theta_c$ no light will be transmitted from region one to region two, it is totally internally reflected. For values of θ_1 greater than the critical angle, the solution for θ_2 will be complex and gives an alternative way of determining if the light undergoes TIR. This is the basic principle that the guiding mechanism of optical fibers are based on.

2.1 Numerical aperture

As the light entering the fiber is coming from another medium, it will refract according to (1). The angle of refraction will affect the angle of incidence at the higher-lower index of refraction interface, see Figure 2. Therefore, the angle of incidence at the fiber's end face is what determines if the light will undergo TIR. Using Figure 2 and (1), the following equation can be set up

$$n \sin\theta_{max} = n_1 \sin(90° - \theta_c) = n_1 \cos\theta_c \tag{3}$$

Squaring both sides and using the trigonometric identity $\cos^2\theta_c = 1 - \sin^2\theta_c$ along with (2) yields

$$n^2 \sin^2\theta_{max} = n_1^2(1 - \frac{n_2^2}{n_1^2}) \Rightarrow \text{NA} = n\sin\theta_{max} = \sqrt{n_1^2 - n_2^2} \tag{4}$$

where the numerical aperture, NA, was defined. Therefore, the fiber's composition will determine how light can be focused into it. Thus, the lenses used to focus light into the fiber must assure that the rays of the beam does not enter in too steep angles, and also that the focused beam is not bigger than the part of the fiber it is supposed to be incident on.

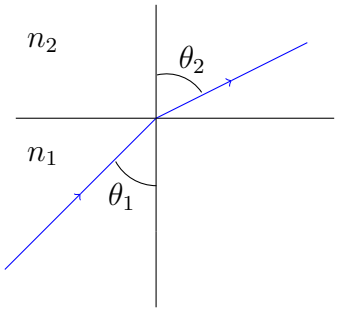

Figure 1: Refraction of light according to Snell's law.

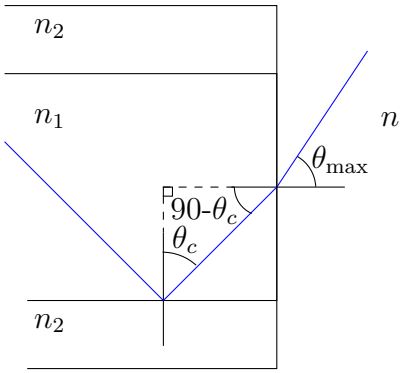

Figure 2: Refraction of light in an optical fiber.

2.2 Single- and multimode fibers

In the classical regime, light propagation is governed by the wave equation derived from Maxwell's equations. Depending on the laser design, the solutions to this wave equation may support several so called transverse modes. The transverse modes are the possible electric field distributions perpendicular to the propagating direction. Hence, the resulting laser beam profile will in general consist of several basic electric field distributions. When incident on an optical fiber, the various electric field distributions will have different guiding properties. Solving Maxwell's wave equation in an optical fiber shows that the number of transverse modes supported by the fiber depends on the numerical aperture, the radius of the medium in which the light is guided and the wavelength of the light [9]. If the fiber only supports one transverse mode it is referred to as a single-mode fiber, otherwise it is called a multimode fiber.

2.3 Fabrication

One way of making optical fibers is by vapor deposition of SiO_2 into a cylindrical preform. A typical preform is 1 m long and has a 2 cm diameter [9]. Different elements are doped into the preform to increase the refractive index of the inner part and decrease it in the outer part, making it possible to obtain TIR. If the fiber is going to be used as an active medium, rare-earth ions are also doped into the preform.

After the preform is done, it is drawn into a thin fiber. The drawing is done such that the ratio between the layers with increased and decreased index of refraction is the same. In this way, the fiber layers can be engineered. Once the fiber is drawn, the innermost part is called the core and the outer part/-s the cladding/-s. To make the fiber more robust it is covered with a plastic coating during the drawing.

2.4 Polarization-maintaining fibers

In practice, there will always be some imperfections in the fabrication and the fiber will not have a perfectly symmetric stress profile. As stress modifies the atom placement, the density will vary which in turn affects the speed at which light can propagate. Since the imperfections are randomly placed throughout the fiber, the polarization of incident light can change.

By introducing so called stress rods, see Figure 3, consisting of modified glass, on each side of the core in the preform, the stress is increased a lot more along the line of the

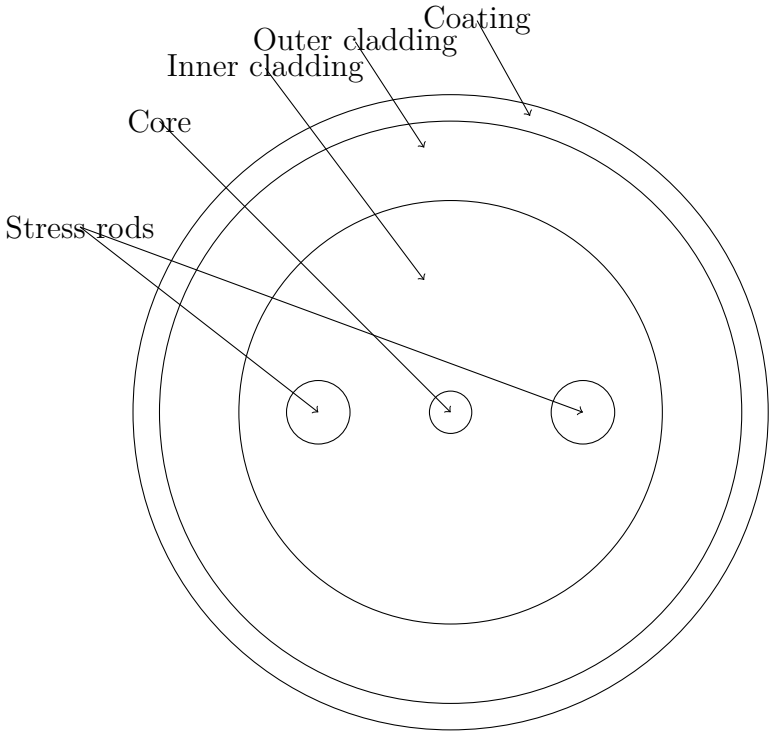

Figure 3: Cross section of a double clad fiber with stress rods.

stress rods than in the perpendicular direction. The induced increase in stress far exceeds the randomly introduced stress. Therefore, the polarization parallel to the stress rods will propagate at a different speed than the perpendicular polarization. Consequently the relative phase between the polarizations will not be preserved, which greatly reduces the ability of disturbances along the fiber to couple both polarizations. This enables the preservation of the polarization of incident light along the line of the stress rods or perpendicular to it.

2.5 Active fibers

Active fibers are optical fibers doped with laser active rare-earth ions. The rare-earth ions introduce electronic energy levels that are populated by absorbing pump light. The excited electrons populating these energy levels are induced to de-excite to the ground level if light of a frequency corresponding to the energy difference between the ground and excited level is incident. The energy difference is released as a photon. This phenomenon is called stimulated emission and generates more photons of the same frequency as they propagate through the fiber. Therefore, active fibers can be used as optical amplifiers and lasers.

Apart from de-excitation of electrons due to stimulated emission, the excited electrons will also spontaneously de-excite as the rare-earth ions seek to lower their energy. This gives the excited level an effective lifetime. The spontaneous depopulation results in light emission, which will also be amplified by inducing stimulated emission. This phenomenon is referred to as amplified spontaneous emission, ASE. Thus, ASE limits the excited electrons that can be used to amplify an incident signal.

There will also be losses due to absorption, impurities and Rayleigh scattering as a result of density fluctuations from the fabrication [9]. These effects, the ASE, the lifetime

and the pump's ability to counteract the depopulation of the excited level, will limit the population in the excited level which in turn limits the amplification.

2.6 Pumping

The most common way of pumping active optical fibers is by coupling a laser diode into one of the fiber ends, called end pumping. If the fiber has a single cladding layer, the pump is focused into the core. Since the core has a diameter of only a few μm, the focused pump must be diffraction limited [8]. Due to the TIR this technique guarantees that the pump is applied throughout the entire fiber, given that it has sufficient power to not be entirely absorbed during its propagation through the fiber.

Usually, diffraction limited pump sources have rather low power. In order to be able to use higher pump powers, cladding pumping was invented. Since the cladding is bigger than the core, it does not require as high beam quality for the pump to be focused into it. As the pump light is guided through the cladding, it will pass the core and thus excite the electrons of the dopants. Cladding pumping requires an inner and an outer cladding, see Figure 3. The inner cladding has a lower index of refraction than the core to confine the signal to the core. The outer cladding has a lower index of refraction than the inner cladding to confine the pump to the inner cladding. Double clad fibers are not commonly used in telecoms as light escaping the core can be guided in the cladding, which can result in interference with the signal propagating in the core.

As the pump is absorbed during its propagation through the fiber it will weaken. This results in that the amount of electrons able to be excited by the pump will decrease from the pump end to the other end, thus yielding a non constant gain along the fiber.

2.7 Angle cleaving

The law of reflection states that the angle of reflection is the same as the incidence angle, relative to the surface normal. For an optical fiber with an end cut at 90°, see Figure 4, this means that the light propagating in the core that is reflected at the end face will change direction and still undergo TIR. The amount of light that is reflected at the fiber end can be calculated using the Fresnel equations [10]. Since the reflected light will also be amplified in active fibers, a reflection of only a few percent can be enough to turn the fiber into a laser cavity. This is undesired for optical amplifiers, since they are only

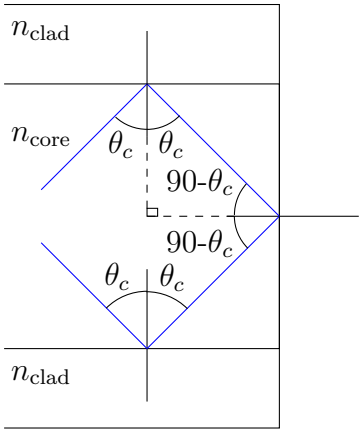

Figure 4: Reflection at the end face of a fiber cleaved at 90°.

to amplify incident light. By cleaving the fiber ends at an angle different from 90°, the light reflected at the end face will have a different angle of incidence to the core-cladding interface. In this way it is possible to reduce the TIR of the end-reflected light.

2.7.1 The effect of angle cleaving on acceptance angles for TIR

Since angle cleaving will change the direction of the fiber end's surface normal, the incidence angles needed for TIR will also change. A cleaving angle of α will make the fiber end's surface normal shift $90° - \alpha$. Tracing the path for a ray undergoing TIR with its last reflection, before reaching the fiber end, at the top of the fiber yields Figure 5a. The angle θ_{max2} was defined in order for easier comparison to the numerical aperture before the angle cleaving. Using Figure 5a and (1), the following equation can be set up

$$n_c \sin(180° - (\theta_c + \alpha)) = n \sin(90° - \alpha + \theta_{\text{max2}}) \tag{5}$$

Solving for θ_{max2} gives

$$\theta_{\text{max2}} = \arcsin\left(\frac{n_c}{n}\sin\left(180° - [\theta_c + \alpha]\right)\right) + \alpha - 90° \tag{6}$$

and is valid until the reflected light from the upper part of the fiber undergoes TIR at the now tilted fiber end face, i.e. while the following condition is fulfilled

$$\frac{n_c}{n}\sin\left(180 - [\theta_c + \alpha]\right) \leq 1 \Rightarrow 180 - \theta_c - \arcsin\frac{n}{n_c} \leq \alpha \tag{7}$$

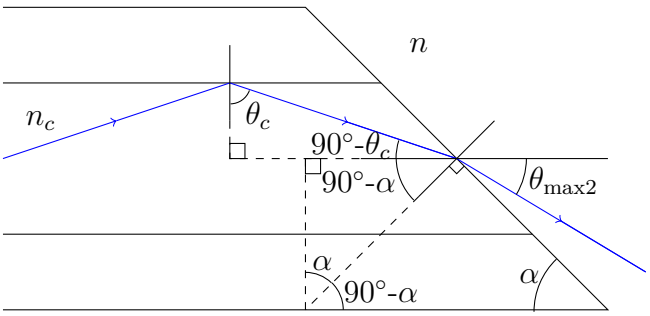

(a) Upper ray undergoing TIR.

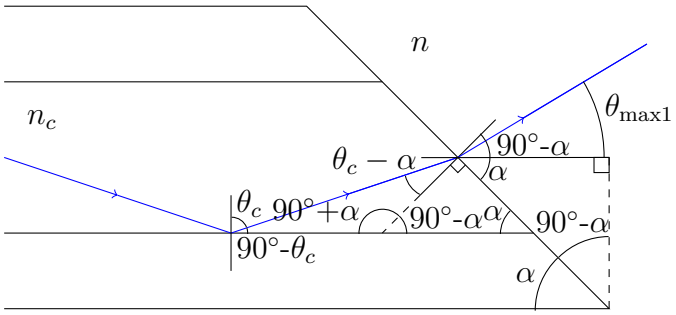

(b) Lower ray undergoing TIR.

Figure 5: Refraction of light at the end of a fiber cleaved at an angle<90°.

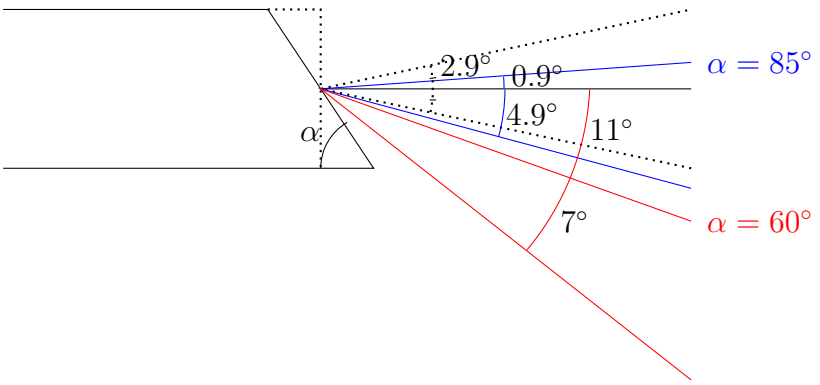

Figure 6: Schematic illustration of skewed acceptance triangles for different cleaving angles in the case of NA=0.05, $n = 1$ and $n_c = 1.4$.

This gives a minimum value of at what angle the fiber can be cleaved to allow incident light having its first reflection at the top of the fiber to undergo TIR.

The light reflected from the bottom of the fiber before reaching the fiber end should be analyzed for two cases, depending on the cleaving angle. The first case is when the light reflected from the bottom of the fiber is still incident on the opposite side of the surface normal at the end face, relative to the light reflected from the top of the fiber. Thus, the second case is when both are incident on the same side of the surface normal. However, both of these analyzes lead to the same result and therefore only the second is detailed here. Using Figure 5b and (1), the following equation can be set up

$$n_c \sin(\theta_c - \alpha) = n \sin(90^\circ - \alpha - \theta_{\text{max1}}) \tag{8}$$

where θ_{max1} was also defined for easier comparison with the numerical aperture before the cleaving. Solving for θ_{max1} gives

$$\theta_{\text{max1}} = 90^\circ - \alpha - \arcsin\left(\frac{n_c}{n}\sin(\theta_c - \alpha)\right) \tag{9}$$

which is valid for

$$\frac{n_c}{n}\sin(\theta_c - \alpha) \leq 1 \Rightarrow \theta_c - \arcsin\left(\frac{n}{n_c}\right) \leq \alpha \tag{10}$$

Figure 6 shows how the rays leading to TIR change as the cleaving angle is decreased. It is seen that the acceptance triangle gets shifted as the cleaving angle decreases. The acceptance cone, which is the 3-D version of the acceptance triangle, will therefore be shifted in the plane of Figure 6 although it will be unaffected in the perpendicular plane. This induced astigmatism; i.e. the diffraction angles, for light coupled out of the fiber, being different in these planes; makes coupling light into the fiber more difficult. Using cylindrical lenses, it is possible to reshape the laser beam, which makes the coupling of light into the angle cleaved fiber more efficient.

3 Models

Although geometric optics is sufficient to understand the most basic guiding properties of optical fibers, it is insufficient for understanding pulse propagation. In this section, two different models for pulse propagation in optical fibers, the generalized nonlinear Schrödinger equation, GNLS, and the rate equations, are introduced.

3.1 Mawell's Equations

The physics governing light in the classical, i.e. non quantum mechanical, regime is contained within Maxwell's equations, presented below in SI-units.

$$\nabla \times \mathbf{E} = -\frac{\partial \mathbf{B}}{\partial t} \tag{11}$$

$$\nabla \times \mathbf{H} = \mathbf{J} + \frac{\partial \mathbf{D}}{\partial t} \tag{12}$$

$$\nabla \cdot \mathbf{D} = \rho \tag{13}$$

$$\nabla \cdot \mathbf{B} = 0 \tag{14}$$

$$\mathbf{D} = \epsilon_0 \mathbf{E} + \mathbf{P} \tag{15}$$

$$\mathbf{B} = \mu_0 \mathbf{H} + \mathbf{M} \tag{16}$$

Where $\mathbf{E}$ is the electric field, $\mathbf{H}$ is the magnetic field, $\mathbf{D}$ is the electric flux density, $\mathbf{B}$ is the magnetic flux density, $\mathbf{J}$ is the current density, $\mathbf{P}$ is the induced electric polarization, $\mathbf{M}$ is the induced magnetic polarization, ρ is the charge density, ϵ_0 is the vacuum permittivity and μ_0 is the vacuum permeability.

Optical fibers do not have free currents, $\mathbf{J} = 0$, nor free charges, $\rho = 0$, and are nonmagnetic, $\mathbf{M} = 0$. Using this and taking the curl of (11) while using (16), (12) and (15) along with the vector calculus identity $\nabla \times \nabla \times \mathbf{E} = \nabla(\nabla \cdot \mathbf{E}) - \nabla^2 \mathbf{E}$ yields

$$\nabla(\nabla \cdot \mathbf{E}) - \nabla^2 \mathbf{E} = -\mu_0 \epsilon_0 \frac{\partial^2 \mathbf{E}}{\partial t^2} - \mu_0 \frac{\partial^2 \mathbf{P}}{\partial t^2} \tag{17}$$

The polarization, $\mathbf{P}$, is the material's response to the electric field, $\mathbf{E}$. Therefore, it basically corresponds to the motion of the bound electrons in the material under influence of the electric field. The oscillating motion of the electrons will depend upon the frequency of the electric field. Thus, it is possible to expand $\mathbf{P}$ in a series of $\mathbf{E}$ with frequency-dependent elements. If the electric field consist of N different frequencies, it can be expressed as

$$\mathbf{E} = \sum_{i=1}^{N} \mathbf{E}(\omega_i) \tag{18}$$

Therefore, a polarization oscillating at a frequency ω can be expressed as

$$\begin{aligned} \frac{\mathbf{P}(\omega)}{\epsilon_0} &= \chi^1(\omega;\omega_1)\mathbf{E}(\omega_1) + \chi^1(\omega;\omega_2)E(\omega_2) + ... \\ &+ \chi^2(\omega;\omega_1,\omega_1)\mathbf{E}(\omega_1)\mathbf{E}(\omega_1) + 2\chi^2(\omega;\omega_1,\omega_2)\mathbf{E}(\omega_1)\mathbf{E}(\omega_2) + ... \\ &+ \chi^3(\omega;\omega_1,\omega_1,\omega_1)\mathbf{E}(\omega_1)\mathbf{E}(\omega_1)\mathbf{E}(\omega_1) + ... + \chi^3(\omega;\omega_2,\omega_2,\omega_1)\mathbf{E}(\omega_2)\mathbf{E}(\omega_2)\mathbf{E}(\omega_1) + ... \end{aligned} \tag{19}$$

where the χ^i-terms are called electric susceptibilities and $\chi^2(\omega;\omega_1,\omega_2)\mathbf{E}(\omega_1)\mathbf{E}(\omega_2) = \chi^2(\omega;\omega_2,\omega_1)\mathbf{E}(\omega_2)\mathbf{E}(\omega_1)$ was used. This expression is valid in the electric dipole approximation and assuming that the medium response to the electric field is both local and instantaneous [9]. That the medium response is local means that the polarization at a given point in the medium is only dependent on the electric field at the same point. This neglects effects such as the ability of the electric field to modify the wavefunctions of nearby electrons. The instantaneous approximation neglects the effect of molecular vibrations.

In order for the frequency-dependent elements, χ^i, to be able to account for all possible frequency combinations they must be tensors. Thus, (19) can be written in tensor notation

$$\begin{aligned}\frac{P_p(\omega)}{\epsilon_0} &= \chi^1_{pq}(\omega;\omega_i)E_q(\omega_i) + \chi^2_{pqr}(\omega;\omega_j,\omega_k)E_q(\omega_j)E_r(\omega_k)+ \\ &\chi^3_{pqrs}(\omega;\omega_l,\omega_m,\omega_n)E_q(\omega_l)E_r(\omega_m)E_s(\omega_n) + ...\end{aligned} \tag{20}$$

where repeated indices are summed over. χ^1 is a second order tensor, i.e. a matrix, which means that the first order approximation of the polarization is linear. Separating the first order approximation from the higher order approximations makes it possible to write

$$\mathbf{P} = \epsilon_0\mathbf{P}_L + \epsilon_0\mathbf{P}_{\text{NL}} = \epsilon_0\chi^1(\omega)\mathbf{E} + \epsilon_0\mathbf{P}_{\text{NL}} \tag{21}$$

where $\mathbf{P}_L$ is the linear and $\mathbf{P}_{\text{NL}}$ is the nonlinear part of the polarization. Using this and (15) in (13) yields

$$0 = \nabla\cdot\mathbf{D} = \nabla\cdot(\epsilon_0\mathbf{E} + \epsilon_0\chi^1(\omega)\mathbf{E} + \epsilon_0\mathbf{P}_{\text{NL}}) = \nabla\cdot(\epsilon_0\epsilon_r(\omega)\mathbf{E} + \epsilon_0\mathbf{P}_{\text{NL}}) \tag{22}$$

where $\epsilon_r(\omega) = 1 + \chi^1(\omega)$ was defined. Assuming a homogenous fiber, $\epsilon_r(\omega)$ will not be spatially dependent and therefore commute with the divergence operator. Since the nonlinear effects are relatively weak in optical fibers [9], the nonlinear polarization's spatial dependence is neglected in presence of that of the electric field. Thus, (22) reduces to

$$\epsilon_0\epsilon_r(\omega)\nabla\cdot\mathbf{E} = 0 \Rightarrow \nabla\cdot\mathbf{E} = 0 \tag{23}$$

Using this result in (17) along with (21) yields

$$\nabla^2\mathbf{E} = \mu_0\epsilon_0\frac{\partial^2\mathbf{E}}{\partial t^2} + \mu_0\frac{\partial^2\mathbf{P}_L}{\partial t^2} + \mu_0\frac{\partial^2\mathbf{P}_{\text{NL}}}{\partial t^2} \tag{24}$$

3.1.1 Further approximations

Assuming that the polarization of the electric field is unchanged throughout the fiber, which in general is not the case but is a good approximation for a fiber with stress rods, the vector notation for the electric field in (24) can be exchanged to a scalar notation, corresponding to the vector component of the electric field parallel to the polarization axis. Also assuming that the electric field is quasi-monochromatic, i.e. $\frac{\Delta\omega}{\omega_0} << 1$ where ω_0 is the carrier frequency and $\Delta\omega$ is the spectral width, it is possible to use the Slowly Varying Envelope Approximation, SVEA, and express the electric field as

$$E(\mathbf{r},t) = \frac{1}{2}[E_0(\mathbf{r},t)e^{-i\omega_0 t} + c.c.] \tag{25}$$

where $E_0(\mathbf{r},t)$ is a slowly varying function relative to the optical period and *c.c.* denotes the complex conjugate of $E_0(\mathbf{r},t)e^{-i\omega_0 t}$. Using this in (20), expanded to third order, along with that χ^2 is zero for silica fibers due to inversion symmetry [9], yields

$$\begin{aligned}
&\frac{P(\omega)}{\epsilon_0} = \chi^1(\omega;\omega_0)\frac{1}{2}[E_0e^{-i\omega_0 t}+c.c.]+\\
&\chi^3(\omega;\omega_0,\omega_0,\omega_0)\frac{1}{2}[E_0e^{-i\omega_0 t}+c.c.]\frac{1}{2}[E_0e^{-i\omega_0 t}+c.c.]\frac{1}{2}[E_0e^{-i\omega_0 t}+c.c.]\\
&=\chi^1(\omega;\omega_0)\frac{1}{2}[E_0e^{-i\omega_0 t}+c.c.]+\chi^3(\omega;\omega_0,\omega_0,\omega_0)\frac{1}{8}\left(E_0^3e^{-i3\omega_0 t}+3|E_0|^2E_0e^{-i\omega_0 t}+c.c.\right)
\end{aligned} \tag{26}$$

The polarization thus have one frequency component at the same frequency as the incident electric field, ω_0, and one at its third harmonic, $3\omega_0$. The third harmonic component requires phase matching to give a significant contribution, which is not commonly designed into optical fibers [9] and is therefore ignored. The polarization will thus only have a component at the frequency ω_0 and the χ-terms will therefore be written as $\chi^i(\omega_0;\omega_0,...) = \chi^i$. Inserting this in the scalar version of (24) yields

$$\begin{aligned}
&\nabla^2\frac{1}{2}[E_0e^{-i\omega_0 t}+c.c.] = \mu_0\epsilon_0\frac{\partial^2}{\partial t^2}\frac{1}{2}[E_0e^{-i\omega_0 t}+c.c.]+\\
&\mu_0\epsilon_0\frac{\partial^2}{\partial t^2}\left[\chi^1\frac{1}{2}[E_0e^{-i\omega_0 t}+c.c.]+\chi^3\frac{1}{2}\left(\frac{3}{4}|E_0|^2E_0e^{-i\omega_0 t}+c.c.\right)\right]\\
&=\mu_0\epsilon_0\frac{\partial^2}{\partial t^2}\left[\left(1+\chi^1+\chi^3\frac{3}{4}|E_0|^2\right)\frac{1}{2}[E_0e^{-i\omega_0 t}+c.c.]\right]
\end{aligned} \tag{27}$$

Since the third order nonlinear response to the electric field is relatively small compared to the linear one [9], the partial derivative acting on $|E_0|^2$ is ignored. Using this and separating the equation into one for E_0 and one for its conjugate yields the following equation

$$\nabla^2[E_0(\mathbf{r},t)e^{-i\omega_0 t}] = \mu_0\epsilon_0\left(1+\chi^1+\chi^3\frac{3}{4}|E_0|^2\right)\frac{\partial^2}{\partial t^2}[E_0(\mathbf{r},t)e^{-i\omega_0 t}] \tag{28}$$

Expressing this equation in cylindrical coordinates, exploiting the fiber's symmetry and using proper boundary conditions for the fiber core and cladding, it can be solved by separation of variables [9]. The solutions can be written as

$$E_0(\mathbf{r},t) = F(r)E_z(z,t) \tag{29}$$

where E_z is the electric field distribution along the fiber and $F(r)$ is a Bessel function, which describes the radial distribution. The number of Bessel functions, of different orders, that satisfy (28) is what determines the number of transverse modes that the fiber can support. As the solution is separable, it is only the z-part that is of any interest for pulse propagation. Therefore, the $F(r)$ part will be discarded in this thesis.

By Fourier analysis it is possible to construct any absolutely integrable function, a property that all functions representing physical signals must have, out of plane waves. Therefore it is instructive to examine the propagation of a plane wave by setting

$$E_z(z,t)e^{-i\omega_0 t} = Ee^{i(Bz-\omega_0 t)} = Ee^{i([B'+iB'']z-\omega_0 t)} \tag{30}$$

where E is a constant amplitude and $B = B' + iB''$ is the propagation constant. This yields

$$\mu_0\epsilon_0\left(1+\chi^1+\chi^3\frac{3}{4}|Ee^{-B''z}|^2\right)\omega_0^2Ee^{i(Bz-\omega_0t)} = [B'+iB'']^2Ee^{i(Bz-\omega_0t)} \tag{31}$$

using $\mu_0\epsilon_0 = \frac{1}{c^2}$, where c is the speed of light in vacuum, while solving for B, and accounting for that the χ^i-terms in general are complex, gives

$$\begin{aligned} B'+iB'' &= \frac{\omega_0}{c}\sqrt{1+\mathrm{Re}(\chi^1)+i\mathrm{Im}(\chi^1)+\frac{3}{4}[\mathrm{Re}(\chi^3)+i\mathrm{Im}(\chi^3)]|Ee^{-B''z}|^2} \\ &= \frac{\omega_0 n(\omega_0)}{c}\sqrt{1+i\frac{\mathrm{Im}(\chi^1)}{n^2(\omega_0)}+\frac{3}{4n^2(\omega_0)}[\mathrm{Re}(\chi^3)+i\mathrm{Im}(\chi^3)]|Ee^{-B''z}|^2} \\ &\approx \frac{\omega_0 n(\omega_0)}{c}\left(1+\frac{1}{2}\left(i\frac{\mathrm{Im}(\chi^1)}{n^2(\omega_0)}+\frac{3}{4n^2(\omega_0)}[\mathrm{Re}(\chi^3)+i\mathrm{Im}(\chi^3)]|Ee^{-B''z}|^2\right)\right) \end{aligned} \tag{32}$$

where the linear refractive index, $n(\omega_0) = \sqrt{1+\mathrm{Re}(\chi^1)}$, was defined and the first order Taylor expansion of the square root was used. The Taylor expansion assumes that the terms in the inner parenthesis are much smaller than 1. Defining the following quantities

$$n_2(\omega_0) = \frac{3}{8n(\omega_0)}\mathrm{Re}(\chi^3) \tag{33}$$

$$\alpha(\omega_0) = \frac{\omega_0}{n(\omega_0)c}\mathrm{Im}(\chi^1) \tag{34}$$

$$\alpha_2(\omega_0) = \frac{3\omega_0}{4n(\omega_0)c}\mathrm{Im}(\chi^3) \tag{35}$$

$$k_0 = \frac{\omega_0}{c} \tag{36}$$

where n_2 is the nonlinear-index coefficient, α is the absorption coefficient, α_2 is the two-photon absorption coefficient, k_0 is the wavenumber at the carrier frequency and using that α_2 is relatively small in silica fibers [9], (30) can be expressed as

$$Ee^{i(Bz-\omega_0t)} = Ee^{-\frac{\alpha(\omega_0)}{2}z}e^{ik_0\left[n(\omega_0)+n_2(\omega_0)\left|Ee^{-\frac{\alpha(\omega_0)}{2}}\right|^2\right]z}e^{-i\omega_0t} \tag{37}$$

where the z part of the exponential has been separated into two for clarity. The first exponential gives a damping of the amplitude, thus corresponding to absorption, while the second exponential gives the acquired phase of the electric field as it propagates. A closer look at the second exponential reveals that the third order nonlinear term gives an intensity dependent phase, since

$$I = \frac{cn(\omega_0)\epsilon_0}{2}|E|^2 \tag{38}$$

where I is the intensity.

3.2 The Generalized Nonlinear Schrödinger Equation

The following section derives the equation governing pulse propagation in optical fibers, the GNLS, in a similar manner as in [11]. This is done by using that the refractive index in an optical fiber consists of an intensity independent and an intensity dependent part.

3.2.1 The Group Velocity

The phase of a plane wave in an optical fiber, see (37), is given by

$$\phi(z,t) = k(\omega, |E|^2)z - \omega t \tag{39}$$

where the 0 subscript was dropped for brevity and where

$$k(\omega, |E|^2) = k_0 \left[n(\omega) + n_2(\omega) \left| E e^{-\frac{\alpha(\omega)}{2}} \right|^2 \right] \tag{40}$$

The phase fronts of the wave will move at the so called phase velocity given by

$$v_p = \frac{dz}{dt} = \frac{\frac{d\phi(z,t)}{dt}}{\frac{d\phi(z,t)}{dz}} = \frac{\omega}{k(\omega, |E|^2)} \tag{41}$$

This equation can be rewritten as

$$v_p k(\omega, |E|^2) - \omega = 0 \tag{42}$$

Differentiating this equation, for when the frequency and wave number of the wave varies as it does when there are several plane waves, yields

$$d\omega - dk(\omega, |E|^2)v_g = 0 \Rightarrow v_g = \frac{d\omega}{dk(\omega, |E|^2)} \tag{43}$$

where the so called group velocity, v_g, was introduced. The group velocity is the velocity at which the resulting envelope of all the plane waves moves.

3.2.2 Derivation of a basic form

The starting point is to Taylor expand the wave number, given by (40), and the absorption about the carrier frequency of the pulse, ω_0,

$$\begin{aligned} k(\omega, |E|^2) &= k_0 \left[n(\omega) + n_2(\omega)|E|^2 \right] = k_L(\omega) + k_{NL}(\omega)|E|^2 \\ &= k_L(\omega_0) + \sum_{n=1}^{\infty} \frac{d^n k_L(\omega_0)}{d\omega^n} \frac{(\omega - \omega_0)^n}{n!} + \left(k_{NL}(\omega_0) + \sum_{m=1}^{\infty} \frac{d^m k_{NL}(\omega_0)}{d\omega^m} \frac{(\omega - \omega_0)^m}{m!} \right) |E|^2 \end{aligned} \tag{44}$$

$$\alpha(\omega) = \alpha(\omega_0) + \sum_{l=1}^{\infty} \frac{d^l \alpha(\omega_0)}{d\omega^l} \frac{(\omega - \omega_0)^l}{l!} \tag{45}$$

It is customary to introduce the nonlinear parameter, γ, and define a new amplitude, A, as

$$\begin{aligned} k_{NL}|E|^2 &= \frac{2\pi n_2(\omega_0)}{\lambda}|E|^2 = \frac{2\pi n_2(\omega_0)}{\lambda} \frac{2}{\epsilon_0 c n(\omega_0) A_{eff}} \frac{\epsilon_0 c n(\omega_0) A_{eff}}{2}|E|^2 \\ &= \left[\gamma = \frac{4\pi n_2(\omega_0)}{\lambda \epsilon_0 c n(\omega_0) A_{eff}}, A = \sqrt{\frac{\epsilon_0 c n(\omega_0) A_{eff}}{2}} E \right] = \gamma |A|^2 \end{aligned} \tag{46}$$

where n_2 is the nonlinear part of the refractive index, related to the χ^3 tensor, expressed in $\frac{\mathrm{m}^2}{\mathrm{V}^2}$ and A_{eff} is the effective mode area, i.e. the cross section area of the fiber that the

guided mode covers. Using (38) it is clear that the absolute square of the new amplitude is the pulse power.

Calling the frequency of the plane wave in (37) ω and expressing it in power amplitude while removing the carrier frequency from it by multiplication with $\mathrm{e}^{-i(k_0 z-\omega_0 t)}$, where k_0 is the linear part of the wavenumber at the carrier frequency ω_0, yields

$$A_{\text{plane}}(z,t) = Ae^{-\frac{\alpha(\omega)}{2}z} e^{i\left(k_L(\omega)-k_L(\omega_0)+\gamma(\omega)\left|Ae^{-\frac{\alpha(\omega)}{2}z}\right|^2\right)z} e^{-i(\omega-\omega_0)t} \tag{47}$$

Examining the partial derivatives with respect to z and t

$$\frac{\partial A_{\text{plane}}}{\partial z} = \left(-\frac{\alpha(\omega)}{2} + i(k_L(\omega) - k_L(\omega_0) + \gamma(\omega)|A_{\text{plane}}|^2)\right) A_{\text{plane}} \tag{48}$$

$$\frac{\partial^n A_{\text{plane}}}{\partial t^n} = \left[-i(\omega-\omega_0)\right]^n A_{\text{plane}} \tag{49}$$

makes it possible to fulfill (44) with the following equation

$$\begin{aligned}\frac{\partial A_{\text{plane}}}{\partial z} = &-\frac{1}{2}\left(\alpha(\omega_0) + \sum_{l=1}^{\infty}\alpha_l \frac{i^l}{l!}\frac{\partial^l}{\partial t^l}\right) A_{\text{plane}} - \left(\sum_{n=1}^{\infty}\beta_n \frac{i^{n-1}}{n!}\frac{\partial^n}{\partial t^n}\right) A_{\text{plane}} \\ &+ \left(i\gamma(\omega_0) + \sum_{m=1}^{\infty}\gamma_m \frac{i^{m-1}}{m!}\frac{\partial^m}{\partial t^m}\right)|A_{\text{plane}}|^2 A_{\text{plane}}\end{aligned} \tag{50}$$

where the following parameters were introduced

$$\beta_n = \tfrac{d^n k_L(\omega_0)}{d\omega^n} \qquad \alpha_l = \tfrac{d^l \alpha(\omega_0)}{d\omega^l} \qquad \gamma_m = \tfrac{2}{\epsilon_0 c n(\omega_0) A_{eff}} \tfrac{d^m K_{NL}(\omega_0)}{d\omega^m} \tag{51}$$

The group velocity, (43), is usually taken as only the derivative of the linear part of the wave number. Thus, $\beta_1 = \frac{dk_L(\omega)}{d\omega} = \frac{1}{v_g}$. The effect of the group velocity is to advance the pulse in time. As the equation is to be solved numerically, it is more convenient to have the pulse maintain a fixed position in time since that requires less time points. This can be achieved by the following coordinate transformation

$$Z = z \quad T = t - \beta_1 z \tag{52}$$

and using that

$$\begin{aligned}\frac{\partial A(Z,T)}{\partial z} &= \frac{\partial A(Z,T)}{\partial Z}\frac{\partial Z}{\partial z} + \frac{\partial A(Z,T)}{\partial T}\frac{\partial T}{\partial z} = \frac{\partial A(Z,T)}{\partial Z} - \beta_1 \frac{\partial A(Z,T)}{\partial T} \\ \frac{\partial A(Z,T)}{\partial t} &= \frac{\partial A(Z,T)}{\partial T}\frac{\partial T}{\partial t} + \frac{\partial A(Z,T)}{\partial Z}\frac{\partial Z}{\partial t} = \frac{\partial A(Z,T)}{\partial T}\end{aligned} \tag{53}$$

Then (50) can be expressed as

$$\begin{aligned}\frac{\partial A}{\partial Z} = &-\frac{1}{2}\left(\alpha(\omega_0) + \sum_{l=1}^{\infty}\alpha_l \frac{i^l}{l!}\frac{\partial^l}{\partial T^l}\right) A - \left(\sum_{n\geq 2}^{\infty}\beta_n \frac{i^{n-1}}{n!}\frac{\partial^n}{\partial T^n}\right) A \\ &+ \left(i\gamma(\omega_0) + \sum_{m=1}^{\infty}\gamma_m \frac{i^{m-1}}{m!}\frac{\partial^m}{\partial T^m}\right)|A|^2 A\end{aligned} \tag{54}$$

This equation is referred to as the Nonlinear Schrödinger Equation, NLS, when only the first term in the second summation is present while the first and third summations are

approximated by their zeroth terms, i.e. $\alpha(\omega_0)$ and $\gamma(\omega_0)$. The reason for this is the resemblance to a Schrödinger equation with a nonlinear potential and the space and time derivatives interchanged. When summation terms of higher order, and also when more terms describing effects not considered here, are present it is instead referred to as the GNLS.

In practice, the third summation is well enough approximated by its two first terms and γ_1 can be approximated by $\frac{\gamma(\omega_0)}{\omega_0}$ for less spectral broadening than 20 THz [9]. The resulting equation then becomes

$$\begin{aligned}\frac{\partial A}{\partial Z} = &-\frac{1}{2}\left(\alpha(\omega_0) + \sum_{l=1}^{\infty}\alpha_l\frac{i^l}{l!}\frac{\partial^l}{\partial T^l}\right)A - \left(\sum_{n\geq 2}^{\infty}\beta_n\frac{i^{n-1}}{n!}\frac{\partial^n}{\partial T^n}\right)A \\ &+ i\gamma(\omega_0)\left(1 + \frac{i}{\omega_0}\frac{\partial}{\partial T}\right)|A|^2A\end{aligned} \tag{55}$$

3.2.3 Including the Raman term

As stated in section 3.1, the instantaneous approximation neglects the effect of molecular vibrations. The vibrational response, also called the Raman response, in silica fibers occur over a duration of 60-70 fs, making its negligence questionable for pulse widths < 1 ps [9]. Including the Raman response amounts to re-expressing (19) and using perturbation theory, the outline of this derivation is given in [9]. However, the resulting equation can be obtained by changing the pulse power term in (55), i.e. $|A|^2$, to its convolution with the Raman response function, $R(T)$, given by

$$R(T) = (1 - f_R)\delta(T) + f_R\frac{\tau_1^2 + \tau_2^2}{\tau_1\tau_2^2}\theta(T)\mathrm{e}^{\frac{-T}{\tau_2}}\sin\left(\frac{-T}{\tau_1}\right) \tag{56}$$

where f_R is the fractional contribution of the Raman response, $\theta(T)$ is the Heaviside step function, τ_1 and τ_2 are parameters to adjust the function to the Raman gain spectrum. The resulting generalized nonlinear Schrödinger equation then takes the form

$$\begin{aligned}\frac{\partial A}{\partial Z} = &-\frac{1}{2}\left(\alpha(\omega_0) + \sum_{l=1}^{\infty}\alpha_l\frac{i^l}{l!}\frac{\partial^l}{\partial T^l}\right)A - \left(\sum_{n\geq 2}^{\infty}\beta_n\frac{i^{n-1}}{n!}\frac{\partial^n}{\partial T^n}\right)A \\ &+ i\gamma(\omega_0)\left(1 + \frac{i}{\omega_0}\frac{\partial}{\partial T}\right)A\int_{-\infty}^{\infty}R(\tau)|A(z, t-\tau)|^2d\tau\end{aligned} \tag{57}$$

3.2.4 The effect of gain dispersion

The first summation on the right hand side of (57) is the result of the frequency dependence of the absorption. Isolating this summation and taking the Fourier transform of the equation yields

$$\frac{\partial\mathcal{A}}{\partial Z} = -\left(\alpha(\omega_0) + \sum_{l=1}^{\infty}\alpha_l\frac{i^l}{l!}(i\omega)^l\right)\mathcal{A} \Rightarrow \mathcal{A}(Z,\omega) = \mathcal{A}(0,\omega)\mathrm{e}^{-\left(\alpha(\omega_0)+\sum_{l=1}^{\infty}\alpha_l\frac{i^{2l}\omega^l}{l!}\right)z} \tag{58}$$

where $\mathcal{A}$ is the Fourier transform of $A(Z_i, t)$ with respect to time. This shows that the frequency components of the pulse will experience different damping, i.e. absorption. The convention of having a negative complex exponential for the carrier frequency in (28)

affect the signs of the expansion terms in (50). Fourier transforming the nth derivative of a function amounts to multiplying the transform of the function with $(i\omega)^n$, as opposed to $(-i\omega)^n$. This is the reason for the alternating signs, due to i^{2l}, in the frequency expansion in the exponential.

3.2.5 The effect of group velocity dispersion

The effects of the second summation's terms in (57) can be analyzed by excluding the other ones yielding

$$\frac{\partial A}{\partial Z} = -\left(\sum_{n\geq 2}^{\infty} \beta_n \frac{i^{n-1}}{n!}\frac{\partial^n}{\partial T^n}\right) A \tag{59}$$

Fourier transforming this equation gives

$$\begin{aligned} &\frac{\partial \mathcal{A}}{\partial Z} = -\left(\sum_{n\geq 2}^{\infty} \beta_n \frac{i^{n-1}}{n!}(i\omega)^n\right) \mathcal{A} \Rightarrow \mathcal{A}(Z,\omega) = \mathcal{A}(0,\omega) e^{i\left(\sum_{n\geq 2}^{\infty} \beta_n \frac{(-1)^n}{n!}\omega^n\right) z} \\ &\Rightarrow A(Z,T) = \int_{-\infty}^{+\infty} \mathcal{A}(0,\omega) e^{i\left(\sum_{n\geq 2}^{\infty} \beta_n \frac{(-1)^n}{n!}\omega^n\right) z} e^{-i\omega T} d\omega \end{aligned} \tag{60}$$

In this way the summation terms introduce additional frequency dependent phase terms. Since β_1 is the inverse group velocity, β_2 is the first order change of the inverse group velocity with frequency, see (51), called the Group Velocity Dispersion, GVD, parameter. Similarly, higher order β-terms give higher order changes of the inverse group velocity with frequency. Non zero $\beta_{n\geq 2}$ terms indicate that the group velocity differ with frequency. This means that the frequency components constituting the pulse envelope will move at different velocities. Thus, the $\beta_{n\geq 2}$ terms will affect the pulse shape. In practice the GVD parameter is usually the dominating term [9]. It is therefore the only term whose effect will be detailed here. By using a Gaussian pulse the effect of the GVD can be clearly seen without too complicated expressions.

$$\begin{aligned} &A(0,T) = e^{-\frac{T^2}{2T_0^2}} \Rightarrow A(0,\omega) = \sqrt{2\pi} T_0 e^{-\frac{\omega^2 T_0^2}{2}} \\ &\Rightarrow A(Z,T) = T_0 \int_{-\infty}^{+\infty} e^{-\frac{\omega^2 T_0^2}{2}} e^{i\frac{\beta_2}{2}\omega^2 z} e^{-i\omega T} d\omega = \frac{T_0}{\sqrt{T_0^2 - i\beta_2 Z}} e^{-\frac{T^2}{2(T_0^2 - i\beta_2 Z)}} \\ &= \frac{T_0}{(T_0^4 + \beta_2^2 Z^2)^{1/4}} e^{i\arg\left((T_0^2 - i\beta_2 z)^{-1/2}\right)} e^{-\frac{T^2(T_0^2 + i\beta_2 z)}{2(T_0^4 + \beta_2^2 Z^2)}} \\ &= \frac{1}{\left(1 + \frac{\beta_2^2 Z^2}{T_0^2}\right)^{1/4}} e^{-\frac{T^2}{2T_0^2\left(1 + \frac{\beta_2^2 Z^2}{T_0^2}\right)} - i\left(\frac{\beta_2 z T^2}{2(T_0^4 + \beta_2^2 Z^2)} - \arg\left((T_0^2 - i\beta_2 z)^{-1/2}\right)\right)} \end{aligned} \tag{61}$$

where $\arg(c)$ denotes the phase of a complex number c. The effect of the GVD parameter is thus seen to spread the pulse and introduce a time dependent phase factor. The instantaneous frequency is given by $-\frac{\partial \phi}{\partial T}$ where ϕ is the phase, the minus comes from the choice $e^{-i\omega_0 T}$ for the carrier frequency. The instantaneous frequency of the pulse, including the phases from the amplitude A and the carrier frequency ω_0, is given by

$$-\frac{\partial \phi}{\partial T} = -\frac{\partial}{\partial T}\left(-\omega_0 T - \frac{\beta_2 Z T^2}{2(T_0^4 + \beta_2^2 Z^2)} - \arg\left((T_0^2 - i\beta_2 Z)^{-1/2}\right)\right) = \omega_0 + \frac{\beta_2 Z T}{T_0^4 + \beta_2^2 Z^2} \tag{62}$$

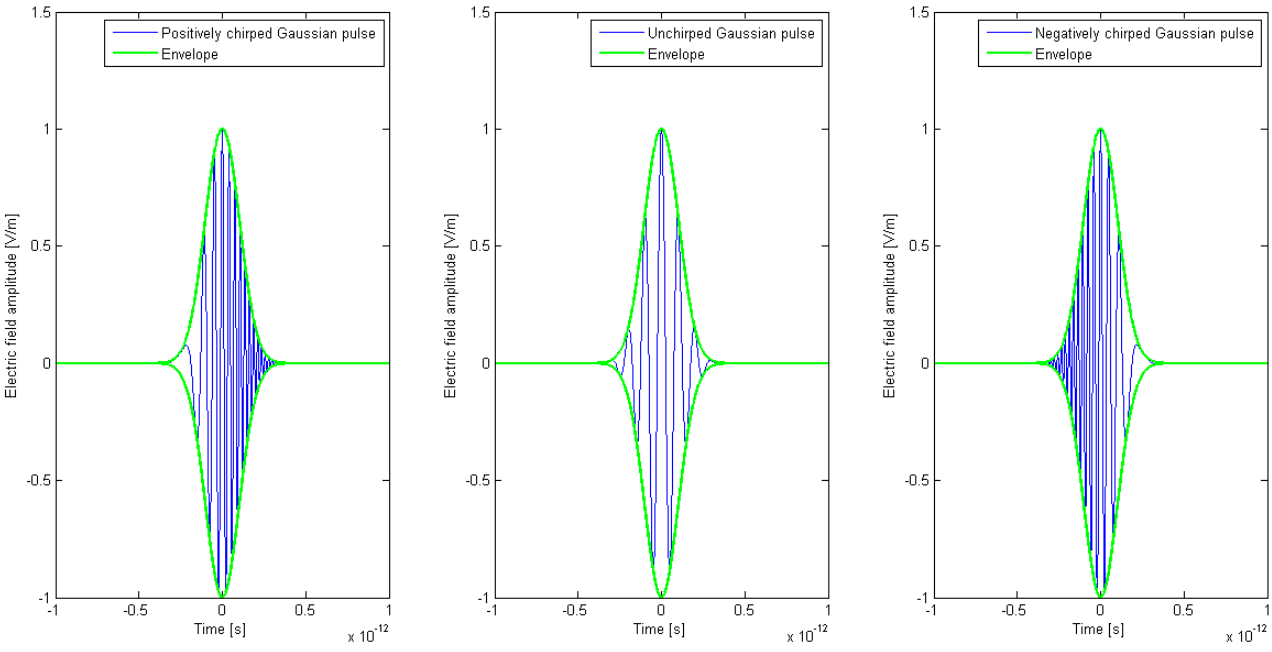

Figure 7: Comparison of chirped and unchirped 170 fs Gaussian pulses with a carrier frequency of 10 THz.

which is time dependent, also referred to as being chirped. The time at which the instantaneous frequency is zero is given by

$$T_{-\frac{\partial\phi}{\partial T}=0} = -\frac{\omega_0(T_0^4 + \beta_2^2 Z^2)}{\beta_2 Z} \tag{63}$$

Beyond this time, the magnitude of the frequency will increase symmetrically in both positive and negative T-direction. In the normal dispersion regime where $\beta_2 > 0$, the pulse will be positively chirped and $T_{-\frac{\partial\phi}{\partial T}=0}$ will be located on the negative T-axis. Since the carrier frequencies are generally quite large, the $T_{-\frac{\partial\phi}{\partial T}=0}$ will be located far out on the negative T-axis where the pulse curve is very close to zero. Therefore, the increase in magnitude of the frequency in negative T-direction beyond $T_{-\frac{\partial\phi}{\partial T}=0}$ is negligible. A positively chirped pulse is therefore said to increase its frequency with time. The opposite situation occurs in the so called anomalous dispersion regime where $\beta_2 < 0$. In this case the pulse is negatively chirped and its frequency is said to decrease over time. Examples of chirped Gaussian pulses are shown in Figure 7. These were obtained by plotting the real part of the pulse amplitudes and including the complex exponential containing the carrier frequency.

3.2.6 The effect of self phase modulation

The effect of the first nonlinear term in (57) is analyzed by isolating it and neglecting the Raman contribution, giving

$$\frac{\partial A}{\partial Z} = i\gamma|A|^2 A \tag{64}$$

Expressing the amplitude as $A(Z,T) = V(Z,T)e^{i\Phi(Z,T)}$ makes it possible to separate this equation in one equation for the real parts and one for the imaginary parts.

$$\frac{\partial V}{\partial Z}e^{i\Phi} + i\frac{\partial \Phi}{\partial Z}Ve^{i\Phi} = i\gamma|V|^2Ve^{i\Phi} \Rightarrow \begin{cases} \frac{\partial V}{\partial Z} = 0 \\ \frac{\partial \Phi}{\partial Z} = \gamma|V|^2 \end{cases} \Rightarrow \begin{cases} V = V_0(T) \\ \Phi = \gamma|V_0(T)|^2 Z + C \end{cases} \tag{65}$$

The amplitude can then be expressed as

$$A(Z,T) = V_0(T)e^{i(\gamma|V_0(T)|^2Z+C)} \Rightarrow A(0,T) = V_0(T)e^{iC} \Rightarrow A(Z,T) = A(0,T)e^{i\gamma|A(0,T)|^2Z} \tag{66}$$

In this way the nonlinear term introduces a power dependent phase, a phenomenon called Self Phase Modulation, SPM. SPM only affects the phase of the pulse while its time profile is unchanged. The SPM leads to an instantaneous frequency, see (62), of

$$-\frac{\partial \phi}{\partial T} = -\frac{\partial}{\partial T}(-\omega_0 T + \Phi) = \omega_0 - \gamma\frac{\partial}{\partial T}|A(0,T)|^2 Z \tag{67}$$

However, unlike (62), this chirp's magnitude increases the further the pulse propagates. This means that the pulse itself gives rise to new frequency components as it propagates. As is evident in (67), the effect of SPM is very dependent on the pulse shape.

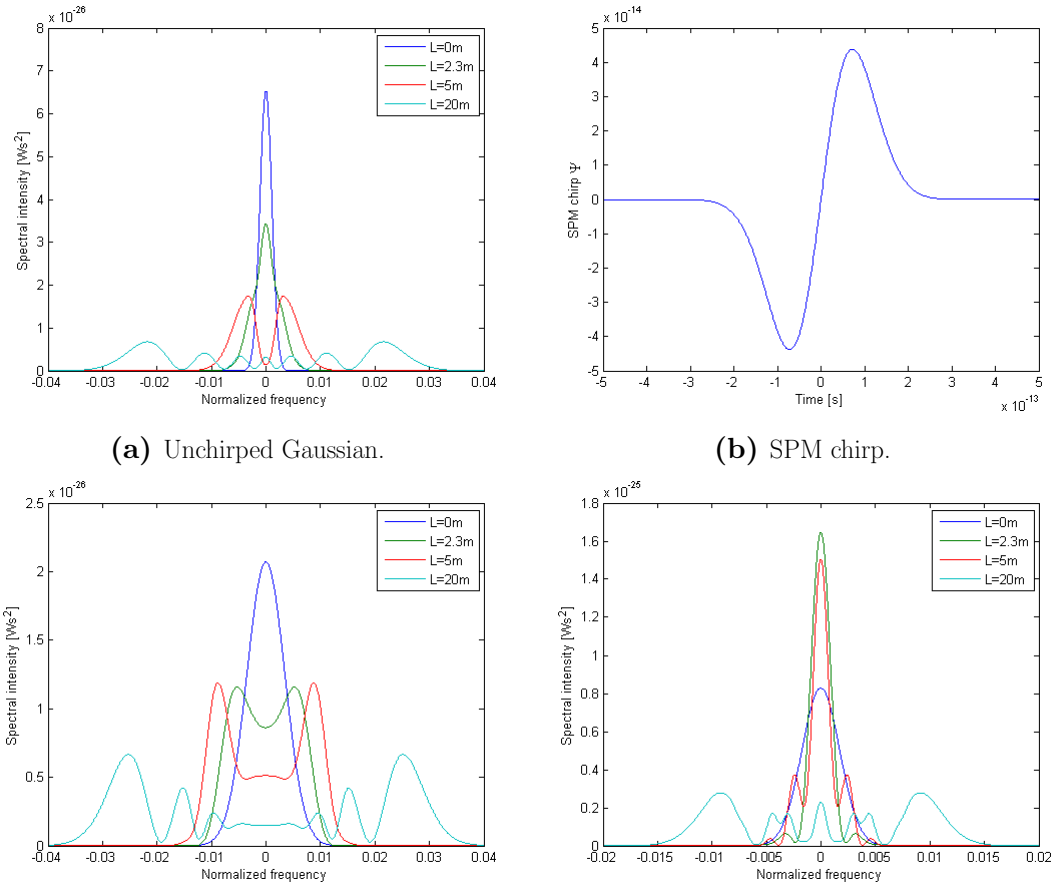

(a) Unchirped Gaussian. **(b)** SPM chirp.

(c) Positively chirped Gaussian, $C = 6$. **(d)** Negatively chirped Gaussian, $C = -6$.

Figure 8: The effect of SPM on 170 fs Gaussian pulses after a propagation distance of L along the fiber with $\gamma = 1$ m^{-1}W^{-1}.

For an unchirped pulse, the new frequency components will broaden the pulse spectrum. In the case of a chirped pulse, the SPM chirp will add to the pulse chirp. These effects are demonstrated for a Gaussian pulse, normalized such that its maximum value is one and such that its carrier frequency is zero:

$$A(0,T) = e^{-(1+iC)\frac{T^2}{4}} \Rightarrow \begin{cases} -\frac{\partial\phi}{\partial T} = \gamma T e^{-\frac{T^2}{2}} = \Psi(T) \\ A(Z,T) = e^{-\frac{T^2}{4}+i\left(-C\frac{T^2}{4}+\gamma e^{-\frac{T^2}{2}}Z\right)} \end{cases} \tag{68}$$

where C is the chirp parameter and the SPM chirp, $\Psi(T)$, was defined. In Figure 8b it is seen that the SPM chirp, apart from at the critical points, has the same value at least at two different times. Thus, there are different times at which the instantaneous frequency is the same. These times correspond to frequency components/waves of the same frequency, but with different phases, that can interfere. The interference results in the oscillations that can be seen in all of the spectra. It is seen that the spectrum of the positively chirped pulse, Figure 8c, broadens faster than the unchirped pulse's spectrum, Figure 8a. The reason for this is that the SPM chirp and the positive chirp have the same sign so that they add without any cancellation. This results in a more chirped pulse which in turn gives a broader spectrum. The negatively chirped pulse, Figure 8d, first narrows the spectrum but then starts broadening it. The narrowing is because of the negatively chirped pulse having the opposite sign of the SPM chirp. They will therefore add with some cancellation and the total chirp will decrease. However, since the SPM chirp increases as the pulse propagates, it eventually gets greater than the negative chirp and the spectrum will start to broaden.

3.2.7 The interplay between GVD and SPM

The parts of the pulse envelope consisting of the new frequency components resulting from SPM will move at different velocities, given by the GVD. Therefore, these frequency components can either result in pulse broadening or narrowing. And since SPM depends on the pulse shape it will be affected by the broadening or narrowing from the GVD. Because of this coupled dependence, the combined effects of GVD and SPM will depend very much on the particular pulse considered. They will also depend a lot on the fiber parameters β_2 and γ. The importance of these parameters can be seen by introducing

$$\tau = \frac{T}{T_0} \quad A(Z,T) = \sqrt{P_0}U(Z,T) \tag{69}$$

where T_0 is the pulse duration and P_0 is the peak pulse power. Using these in the GNLS, (57), with $n = 2$ and only including the terms for GVD and SPM yields

$$\frac{\partial U}{\partial Z} = -i\frac{\beta_2}{2T_0^2}\frac{\partial^2 U}{\partial \tau^2} + i\gamma P_0|U|^2U = -i\frac{\text{sgn}(\beta_2)}{2L_D}\frac{\partial^2 U}{\partial \tau^2} + i\frac{1}{L_{NL}}|U|^2U \tag{70}$$

where the dispersion length, L_D, and the nonlinear length, L_{NL}, were defined as

$$L_D = \frac{T_0^2}{|\beta_2|} \quad L_{NL} = \frac{1}{\gamma P_0} \tag{71}$$

Defining their ratio as

$$N^2 = \frac{L_D}{L_{NL}} = \frac{T_0^2\gamma P_0}{|\beta_2|} \tag{72}$$

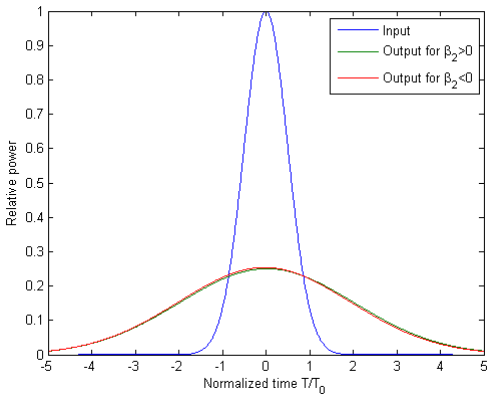

(a) Time profiles for N^2= 0.026.

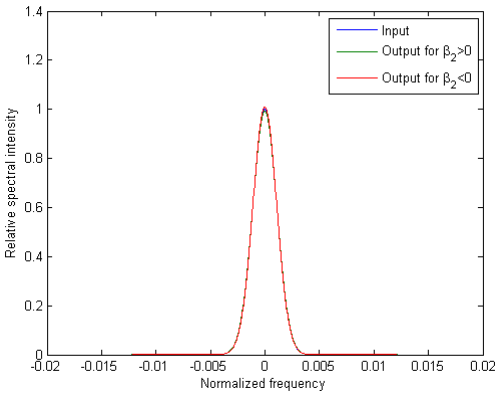

(b) Spectra for N^2= 0.026.

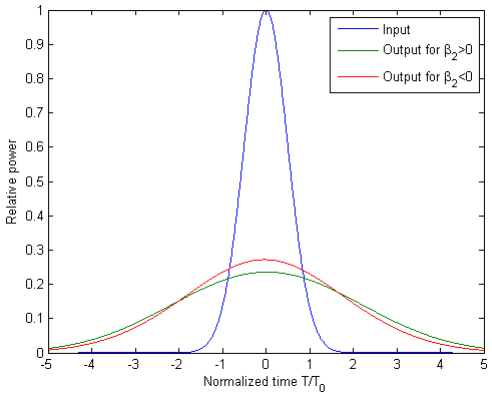

(c) Time profiles for N^2= 0.26.

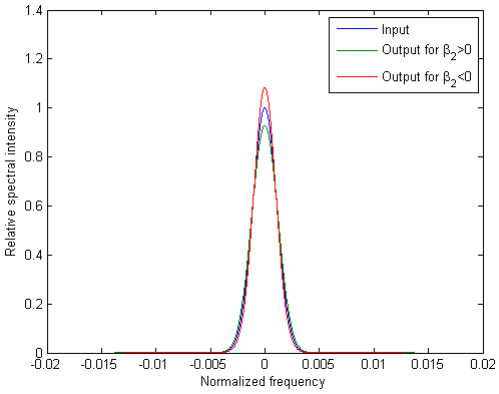

(d) Spectra for N^2= 0.26.

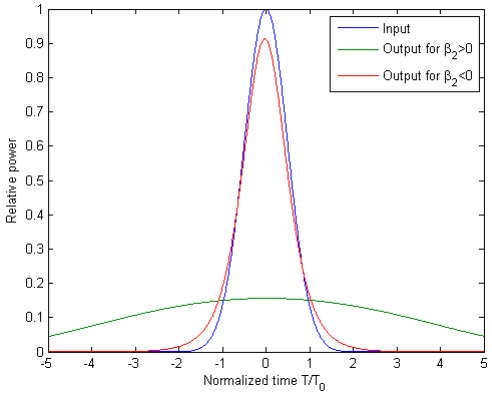

(e) Time profiles for N^2= 2.6.

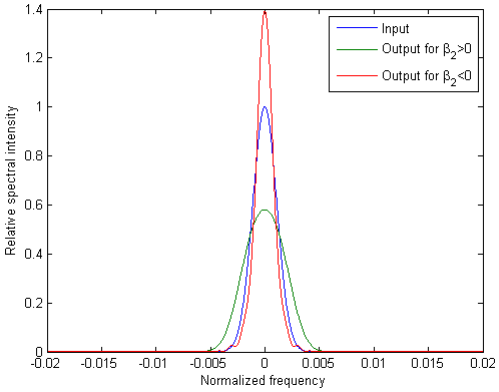

(f) Spectra for N^2= 2.6.

Figure 9: Comparison between output pulse and spectrum, normalized by the top values of the input Gaussian's time profile and spectrum, propagated 1 m for different values of N^2 in the normal and anomalous dispersion regime.

gives a quantity for the relative strength of the GVD and SPM. It follows from (70) that the smallest of L_D and L_{NL} will give the most dominating term. Therefore, GVD will dominate if $N \ll 1$ and SPM if $N \gg 1$. Also note that the sign of β_2 will be of importance.

In Figure 9 three different situations are shown for an unchirped 15 fs Gaussian input pulse. It is seen that for $N^2 = 0.026$ the dispersion regime does not make much difference, since the nonlinear contribution does not yield enough SPM for the dispersion regimes to respond different to. When $N^2 = 0.262$ it is seen that the anomalous regime gives spectral narrowing and less pulse broadening than the normal regime which gives spectral broadening. In the case of $N^2 = 2.6$ the pulse in the anomalous regime has narrowed its spectrum while the pulse in the normal regime has broadened its spectrum. The difference in pulse broadening is also clearly apparent for the time profiles.

3.2.8 The effect of self-steepening

Isolating the term in (57) stemming from the power dependence of the refractive index yields

$$\frac{\partial A}{\partial Z} = -\frac{\gamma(\omega_0)}{\omega_0}\frac{\partial}{\partial T}(|A|^2 A) \tag{73}$$

Since this equation is nonlinear, it cannot rigorously be solved using Fourier analysis. However, considering a very slowly variating power envelope, with respect to the optical frequency, the basic influence of this term can be analyzed by initially treating the pulse power, $|A|^2$, as being constant. The constancy of the pulse power makes it possible to

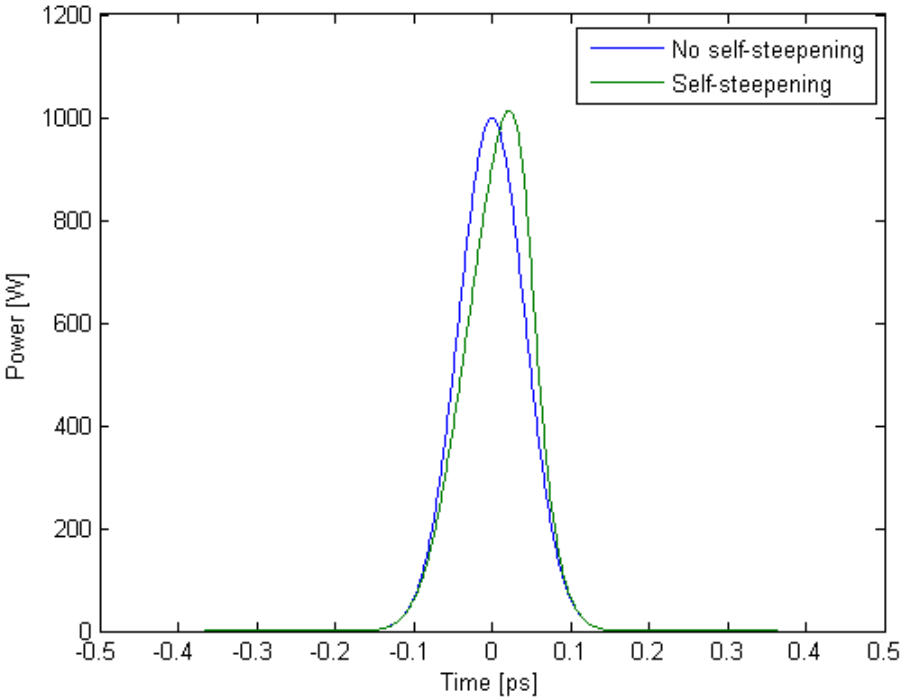

Figure 10: The effect of self-steepening for a 150 fs Gaussian pulse propagated 6 m in a fiber with $\gamma = 5 \cdot 10^{-4}$ $\mathrm{W^{-1}m^{-1}}$.

Fourier transform the equation and get

$$\frac{\partial \mathcal{A}}{\partial Z} = -\frac{\gamma(\omega_0)}{\omega_0} i\omega |A|^2 \mathcal{A} \Rightarrow \mathcal{A} = \mathrm{e}^{-i\omega \frac{\gamma(\omega_0)}{\omega_0}|A|^2 z}\mathcal{A} \Rightarrow A = A\left(T - \frac{\gamma(\omega_0)}{\omega_0}|A|^2 z\right) \tag{74}$$

which implies that parts of the pulse with higher power will undergo more positive time translation, i.e. experience more lag, than parts with lower power. This suggests that the pulse tails will move faster than the peak. The result is that the trailing pulse edge will get steeper while the front pulse edge gets less steep. This situation is referred to as self-steepening and is illustrated in Figure 10.

3.2.9 The Raman effect

Introducing the Raman term in section 3.2.3 amounted to an exchange of the pulse power, $|A|^2$, for its convolution with the Raman response function, $R(t)$. Convolutions give the area of the product between two functions as one is translated relative to the other. Therefore, the Raman convolution can be interpreted as the result of the interaction between the pulse power envelope and the molecular vibrations.

The actual Raman effect consists of a photon being converted into another photon with lower energy, i.e. longer wavelength/lower frequency, and a phonon, i.e. a lattice vibration. This means that the Raman convolution will introduce asymmetry in the spectrum by shifting energy towards lower frequencies. This is illustrated in Figure 11 by comparing the effects on a 150 fs pulse only including the second last terms in (55) and (57). The reversed phenomenon, i.e. when a phonon combines with a photon to generate a higher frequency photon, is referred to as the anti-Stokes effect. As the anti-Stokes effect rarely occurs [9], it will not be included in this analysis.

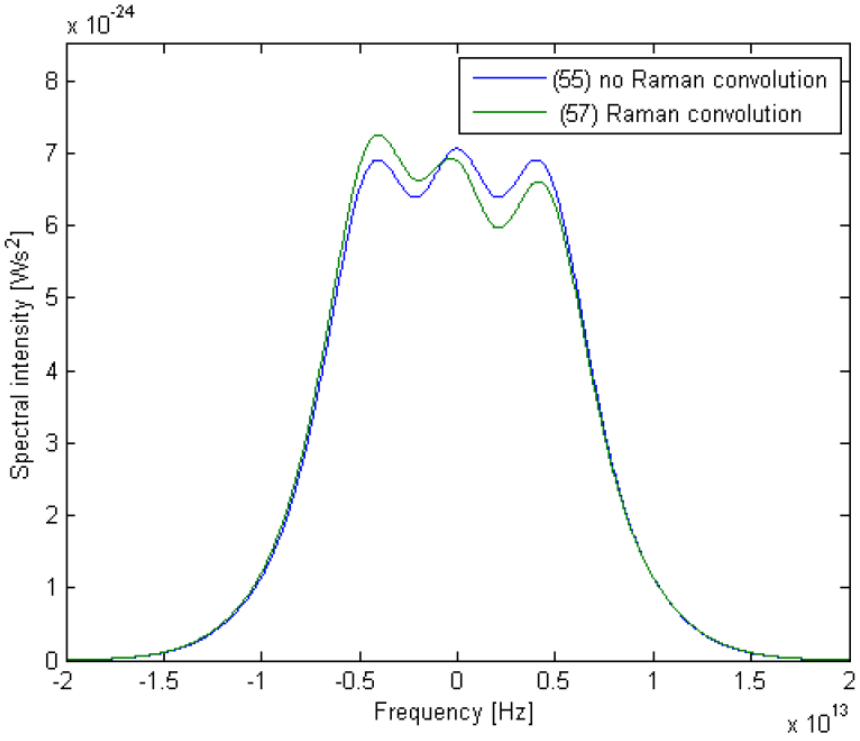

Figure 11: The effect of the Raman convolution on a 150 fs Gaussian pulse propagated 6 m in a fiber with $\gamma = 5 \cdot 10^{-4}$ $\mathrm{W}^{-1}\mathrm{m}^{-1}$.

3.3 The Rate Equations

Modeling the two stark split manifolds of the doped Yb-ions as two effective energy levels, with electron population densities N_1 and N_2 for the effective ground and excited level respectively, spatially dependent rate equations can be set up. These equations describe the power propagation and the electron energy level population along the fiber.

The power propagation will depend on the amount of light that is absorbed by the lower level and emitted by the upper level, as well as on the fiber losses. Assuming a uniform transverse power distribution, a reasonable approximation for a single mode fiber, the transverse profile can be neglected as far as the power propagation along the fiber is concerned. In this case, the following equation can be set up

$$\frac{\partial P_\lambda}{\partial z} = \Gamma \left(\sigma_e(\lambda)N_2 - \sigma_a(\lambda)N_1\right) P_\lambda - \eta P_\lambda \tag{75}$$

where P_λ is the optical power at a given wavelength λ, $\sigma_e(\lambda)$ is the emission cross section at that wavelength which gives a measure of how probable the emission is, $\sigma_a(\lambda)$ is the absorption cross section, η represent the fiber losses and Γ is the overlap factor. The overlap factor represents how well the guided light overlaps with the doped rare-earth ions in the core.

Since propagating light will induce both emission and absorption, the power will vary with time. Taking this into account along with the light's phase velocity, $v_p(\lambda)$, yields

$$\frac{\partial P_\lambda}{\partial z} + \frac{1}{v_p(\lambda)}\frac{\partial P_\lambda}{\partial t} = \Gamma \left(\sigma_e(\lambda)N_2 - \sigma_a(\lambda)N_1\right) P_\lambda - \eta P_\lambda \tag{76}$$

The change of the upper level population with respect to time will depend on the upper level life time for the electrons, as well as on the amount of electrons raised to the upper level due to photon absorption and depopulation due to stimulated emission. This can be expressed as

$$\frac{\partial N_2}{\partial t} = K(\lambda)\Gamma \left(\sigma_e(\lambda)N_2 - \sigma_a(\lambda)N_1\right) P_\lambda - \frac{N_2}{\tau} \tag{77}$$

where τ is the upper level life time and $K(\lambda)$ converts the power into number of photons per area per time. Since the light of concern is propagating in the core, the area to be divided by is the core area, A_c. Dividing the power by the energy gives the number of photons per time. Thus, $K(\lambda)$ can be exchanged for its constituents

$$\frac{\partial N_2}{\partial t} = \frac{\Gamma\lambda}{hcA_c} \left(\sigma_e(\lambda)N_2 - \sigma_a(\lambda)N_1\right) P_\lambda - \frac{N_2}{\tau} \tag{78}$$

where h is Planck's constant and the relation for the photon energy $\mathrm{E_{photon}} = \frac{hc}{\lambda}$ was used.

3.3.1 Accounting for amplified spontaneous emission

The spontaneously emitted power can be expressed with the photon energy $\mathrm{E_{photon}} = \frac{hc}{\lambda} = hf$, where f is the frequency, and the upper level life time, τ,

$$P_{\mathrm{SE}} = \frac{hf}{\tau} \tag{79}$$

where SE stands for spontaneous emission. The probability that the de-excitation occurs at a given frequency is described by the so called normalized line shape $g(f - f_0)$, where

f_0 is the frequency at which the function is centered, integrated over a frequency range. Using a small frequency range, the integral can be approximated by the multiplication $g(f - f_0)\Delta f$. As the spontaneously emitted light in general occur at more than one wavelength, several propagation equations are needed. The frequency difference between the frequencies that are assigned their own propagation equations is what will constitute the frequency range Δf. Since the propagation equations are only concerned with the z-direction, the dopants at each infinitesimal transverse plane are accounted for by multiplying the population density by the core area. Using this reasoning and that the amount of spontaneous emission will depend on the population of excited electrons, the following term for the guided part of the spontaneously emitted power, commonly referred to as amplified spontaneous emission, ASE, can be obtained

$$g(f - f_0)\Delta f \frac{hf}{\tau} N_2 r_c^2 \pi$$

where r_c is the core radius. The spontaneously emitted light will be sent out in random directions and will not in general undergo TIR. Thus, only a fraction, F, of the spontaneously emitted light will be guided. The number of supported fiber modes, m, must also be taken into account. Therefore, a more complete term describing ASE is given by

$$g(f - f_0)\Delta f \frac{hf}{\tau} N_2 m \Gamma F r_c^2 \pi$$

Using that the fiber used in this master thesis is single mode, i.e. $m = 1$, and obtaining the expression for F from the local capture fraction in [12] gives

$$g(f - f_0)\Delta f \frac{hf}{\tau} N_2 \Gamma \frac{\lambda^2}{4\pi n^2}$$

where λ is the wavelength of the spontaneously emitted light and n is the refractive index of the core. Using the relation between the normalized line shape and cross-section along with the expression for the inverse life time of spontaneous emission in [13], the following term for the ASE is obtained

$$\Gamma \sigma_e(\lambda) N_2 \Delta f \frac{2hc}{\lambda}$$

Lastly, re-expressing Δf by

$$\frac{df}{d\lambda} = \frac{d}{d\lambda}\left(\frac{c}{\lambda}\right) = -\frac{c}{\lambda^2} \Rightarrow \Delta f = \frac{c}{\lambda^2}\Delta\lambda \tag{80}$$

gives the following term accounting for ASE

$$P_{\text{ASE}} = \Gamma \sigma_e(\lambda) N_2 \frac{2hc^2 \Delta\lambda}{\lambda^3} \tag{81}$$

3.3.2 Resulting rate equations

The pump light and the light to be amplified make up two different signals. Taking this and that they may contain several wavelengths each into account gives the following spatially dependent rate equations

$$\begin{aligned} \frac{\partial N_2}{\partial t} &= \frac{\Gamma_p}{hcA_c} \sum_{j=1}^{J} \lambda_j^p [\sigma_a(\lambda_j^p) N_1 - \sigma_e(\lambda_j^p) N_2] P_p(\lambda_j^p) \\ &+ \frac{\Gamma_s}{hcA_c} \sum_{k=1}^{K} \lambda_k^s [\sigma_a(\lambda_k^s) N_1 - \sigma_e(\lambda_k^s) N_2] P_s^{\pm}(\lambda_k^s) - \frac{N_2}{\tau} \end{aligned} \tag{82}$$

$$N_1 = N_T - N_2 \tag{83}$$

$$\frac{\partial P_p^{\pm}(\lambda_j^p)}{\partial z} \pm \frac{1}{v_p(\lambda_j^p)} \frac{\partial P_p^{\pm}(\lambda_j^p)}{\partial t} = \pm \left(\Gamma_p [\sigma_e(\lambda_j^p) N_2 - \sigma_a(\lambda_j^p) N_1] P_p^{\pm}(\lambda_j^p) - \eta_p P_p^{\pm}(\lambda_j^p) \right) \tag{84}$$

$$\begin{aligned} \frac{\partial P_s^{\pm}(\lambda_k^s)}{\partial z} \pm \frac{1}{v_p(\lambda_k^s)} \frac{\partial P_s(\lambda_k^s)}{\partial t} = \pm \Big(& \Gamma_s [\sigma_e(\lambda_k^s) N_2 - \sigma_a(\lambda_k^s) N_1] P_s^{\pm}(\lambda_k^s) - \eta_s P_s^{\pm}(\lambda_k^s) \\ & + \Gamma_s \sigma_e(\lambda_k^s) N_2 \frac{2hc^2 \Delta\lambda}{[\lambda_k^s]^3} \Big) \end{aligned} \tag{85}$$

where η_p is the pump loss, η_s is the signal loss, N_T is the doping concentration which is assumed to be constant throughout the fiber, $P_p^{\pm}$ is the pump power, $P_s^{\pm}$ are the signal power of the forward, $+$, and backward, $-$, propagating beams due to reflection at the fiber end and/or counter propagating beams.

3.3.3 Gain saturation

As mentioned earlier, the induced de-excitation of the excited electrons in the doped ions is what adds more photons to the signal that is to be amplified. Given that there is a finite amount of dopants, there will also be a finite amount of photons that can be added to a signal. Thus, the photons added to more powerful signals, containing more photons,

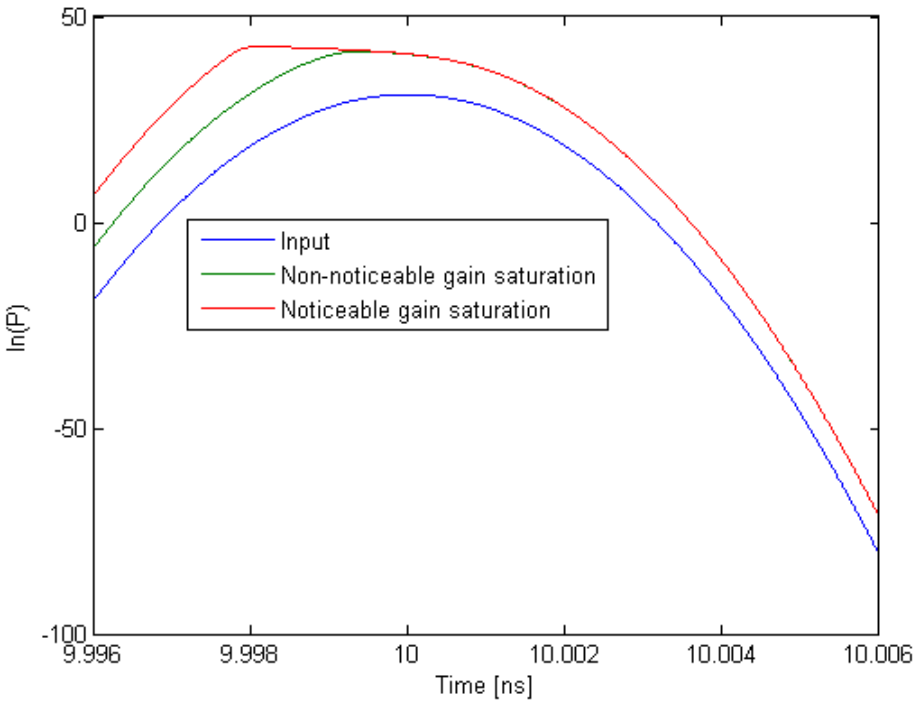

Figure 12: Logarithmic plot, for easier comparison, of the power profile of a Gaussian pulse experiencing gain saturation.

will constitute smaller fractions of the signals' total number of photons, i.e. more powerful signals will experience less gain. This situation is referred to as gain saturation.

Apart from reducing the gain, gain saturation can also lead to pulse distortion. This happens when the de-excitation due to the leading edge results in too few excited electrons to amplify the trailing edge by an equal amount. As the pulse is further amplified, this effect becomes more pronounced.

The effect of gain saturation on a 1 ps monochromatic Gaussian pulse is showed in Figure 12. In this figure it is seen that the trailing edge reaches a maximum level, where the green and red graphs overlap, beyond which it cannot be further amplified. The leading part however, will be further amplified which leads to pulse distortion. This distortion alters the pulse shape, which can be seen by noting that the red graph does not have a Gaussian profile.

4 Numerical Analysis

As it is only possible to obtain analytic solutions for the GNLS and the rate equations in some special cases, it will in general not be possible to solve the coupling between the two models analytically. Therefore, they must be solved numerically. In this section, the numerical approach used for solving the coupling between the two models is outlined.

4.1 Solving the GNLS with a fourth-order Runge-Kutta in the Interaction Picture Method

This method uses a concept, similar to the interaction picture from Quantum Mechanics, to express the GNLS, (57), in a such a way that it is solvable using a fourth-order Runge-Kutta scheme [14].

4.1.1 The quantum mechanical interaction picture

The interaction picture is applicable when the Hamiltonian, $\hat{H}$, can be divided into a time-dependent and a time-independet part.

$$\hat{H} = \hat{H}_1 + \hat{H}_2(t) \tag{86}$$

A Schrödinger state vector, $|a\rangle$, is transformed into an interaction state vector, $|a\rangle^I$, by multiplying it by the following complex exponential

$$|a\rangle^I = \mathrm{e}^{i\frac{\hat{H}_1 t}{\hbar}} |a\rangle \tag{87}$$

where $\hbar = \frac{h}{2\pi}$. Taking the time derivative of the interaction state vector and using the chain rule for differentiation as well as the Schrödinger equation, $i\hbar\frac{\partial}{\partial t}|a\rangle = \hat{H}|a\rangle$, results in an interaction picture Schrödinger equation.

$$\frac{\partial}{\partial t}|a\rangle^I = -\frac{i}{\hbar}\mathrm{e}^{i\frac{\hat{H}_1 t}{\hbar}}\hat{H}_2(t)|a\rangle = \frac{1}{i\hbar}\mathrm{e}^{i\frac{\hat{H}_1 t}{\hbar}}\hat{H}_2(t)\mathrm{e}^{-i\frac{\hat{H}_1 t}{\hbar}}\mathrm{e}^{i\frac{\hat{H}_1 t}{\hbar}}|a\rangle = \frac{1}{i\hbar}H^I|a\rangle^I \Rightarrow i\hbar\frac{\partial}{\partial t}|a\rangle^I = H^I|a\rangle^I \tag{88}$$

Where the interaction Hamiltonian was defined as

$$H^I = \mathrm{e}^{i\frac{\hat{H}_1 t}{\hbar}}\hat{H}_2(t)\mathrm{e}^{-i\frac{\hat{H}_1 t}{\hbar}} \tag{89}$$

Working in the eigen basis, $\{|b\rangle\}$, of the time-independet part of the original Hamiltonian yields coupled differential equations for the expansion coefficents of $|a\rangle^I$ in $\{|b\rangle\}$. After solving these equations, the Schrödinger state vector is then obtained by multiplying the interaction state vector, now expressed in $\{|b\rangle\}$, by the conjugate of the complex exponential used to transform the Schrödinger state vector.

4.1.2 Applying the concept to the GNLS

The right hand side of the GNLS, (57), can be divided into a linear and a nonlinear part with respect to the amplitude A. The linear part represents the effects of gain dispersion and GVD while the nonlinear part represents SPM, self-steepening and the Raman effect. In this way (57) can be expressed as:

$$\frac{\partial A}{\partial Z} = \left(\hat{D} + \hat{N}\right)A \tag{90}$$

where $\hat{D}$, the dispersion operator, and $\hat{N}$, the nonlinear operator, are given by

$$\begin{aligned}\hat{D} &= -\frac{1}{2}\left(\alpha(\omega_0) + \sum_{l=1}^{\infty}\alpha_l \frac{i^l}{l!}\frac{\partial^l}{\partial T^l}\right) - \left(\sum_{n\geq 2}\beta_n \frac{i^{n-1}}{n!}\frac{\partial^n}{\partial T^n}\right) \\ \hat{N} &= i\gamma(\omega_0)\frac{1}{A}\left(1 + \frac{i}{\omega_0}\frac{\partial}{\partial T}\right) A\int_{-\infty}^{\infty} R(\tau)|A(z,t-\tau)|^2 d\tau\end{aligned} \tag{91}$$

The dispersion operator is used, like the time-independent part of the Hamiltonian, to transform the amplitude A into an interaction amplitude A^I in the following way

$$A^I = \mathrm{e}^{-(Z-Z')\hat{D}}A \tag{92}$$

where Z' is the separation distance between the normal and interaction pictures and can be chosen arbitrarily. Taking the partial derivative with respect to Z of the interaction amplitude and using the chain rule for differentiation along with (90) yields

$$\frac{\partial A^I}{\partial Z} = \mathrm{e}^{-(Z-Z')\hat{D}}\hat{N}A = \mathrm{e}^{-(Z-Z')\hat{D}}\hat{N}\mathrm{e}^{(Z-Z')\hat{D}}\mathrm{e}^{-(Z-Z')\hat{D}}A = N^I A^I \tag{93}$$

where the interaction nonlinear operator, N^I, was defined as

$$N^I = \mathrm{e}^{-(Z-Z')\hat{D}}\hat{N}\mathrm{e}^{(Z-Z')\hat{D}} \tag{94}$$

As will be seen in section 4.1.4, (93) has a suitable form to be solved by a fourth-order Runge-Kutta method.

4.1.3 The Fourth-Order Runge-Kutta Method

A system of first order ordinary differential equations, all having the same dependent variable, can be written like

$$\frac{d\mathbf{y}}{dz} = \mathbf{f}(\mathbf{y}, z) \tag{95}$$

The easiest way to numerically solve this type of equations, is to approximate the derivative by its definition and using a small step, Δz, instead of the limit. This is equivalent to approximate the solutions, $\mathbf{y}$, by their Taylor expansions truncated after two terms. The truncation leads to an error proportional to Δz^2 each time the method is used, ie. each time a small step is taken. The number of steps will be given by $n = \frac{z_{\mathrm{end}} - z_{\mathrm{start}}}{\Delta z} \propto \frac{1}{\Delta z}$ and thus the global error will be proportional to Δz.

The fourth-order Runge-Kutta method, RK4, is a more refined way of approximating the derivative, and has a global error proportional to Δz^4. This method is given by [15]

$$\begin{aligned}\mathbf{k}_1 &= \Delta z\mathbf{f}(\mathbf{y}_i, z_i) \\ \mathbf{k}_2 &= \Delta z\mathbf{f}(\mathbf{y}_i + \mathbf{k}_1/2, z_i + \Delta z/2) \\ \mathbf{k}_3 &= \Delta z\mathbf{f}(\mathbf{y}_i + \mathbf{k}_2/2, z_i + \Delta z/2) \\ \mathbf{k}_4 &= \Delta z\mathbf{f}(\mathbf{y}_i + \mathbf{k_3}, z_i + \Delta z) \\ \mathbf{y}_{i+1} &= \mathbf{y}_i + [\mathbf{k}_1 + 2(\mathbf{k}_2 + \mathbf{k}_3) + \mathbf{k}_4]/6\end{aligned} \tag{96}$$

where $\mathbf{y}_i = \mathbf{y}(z_i)$, $\mathbf{y}_{i+1} = \mathbf{y}(z_{i+1})$ and $z_{i+1} = z + \Delta z$.

4.1.4 RK4 applied to the GNLS in the Interaction Picture

The GNLS in the interaction picture, (93), has the same form as (95), which means that the RK4 method can be used to solve it. Applying (96) to (93) and using the definitions of the interaction nonlinear operator, (94), and the interaction amplitude, (92), gives

$$\begin{aligned}
k_1 &= \Delta Z \mathrm{e}^{-(Z_i-Z')\hat{D}} \hat{N}(A(Z_i,T))A(Z_i,T) \\
k_2 &= \Delta Z \mathrm{e}^{-(Z_i+\Delta Z/2-Z')\hat{D}} \hat{N}(\mathrm{e}^{(Z_i+\Delta Z/2-Z')\hat{D}}[A^I(Z_i,T)+k_1/2])\mathrm{e}^{(Z_i+\Delta Z/2-Z')\hat{D}}[A^I(Z_i,T)+k_1/2] \\
k_3 &= \Delta Z \mathrm{e}^{-(Z_i+\Delta Z/2-Z')\hat{D}} \hat{N}(\mathrm{e}^{(Z_i+\Delta Z/2-Z')\hat{D}}[A^I(Z_i,T)+k_2/2])\mathrm{e}^{(Z_i+\Delta Z/2-Z')\hat{D}}[A^I(Z_i,T)+k_2/2] \\
k_4 &= \Delta Z \mathrm{e}^{-(Z_i+\Delta Z-Z')\hat{D}} \hat{N}(\mathrm{e}^{(Z_i+\Delta Z-Z')\hat{D}}[A^I(Z_i,T)+k_3])\mathrm{e}^{(Z_i+\Delta Z-Z')\hat{D}}[A^I(Z_i,T)+k_3] \\
A^I(Z_i+\Delta Z,T) &= A^I(Z_i,T)+[k_1+2(k_2+k_3)+k_4]/6
\end{aligned} \tag{97}$$

Choosing the arbitrary parameter as $Z' = Z_i + \Delta Z/2$ eliminates the exponentials in k_2 and k_3. The amplitude in the normal picture is obtained by multiplying the interaction amplitude by the positive version of the exponential in (92). Multiplying k_4 with this exponential cancels k_4's first exponential, making it possible to redefine it along with the equation for $A^I(Z_i + \Delta Z, T)$. All of this leads to the following method for obtaining $A(Z_i + \Delta Z, T)$

$$\begin{aligned}
A^I(Z_i,T) &= \mathrm{e}^{\frac{\Delta Z}{2}\hat{D}} A(Z_i,T) \\
k_1 &= \Delta Z \mathrm{e}^{\frac{\Delta Z}{2}\hat{D}} \hat{N}(A(Z_i,T))A(Z_i,T) \\
k_2 &= \Delta Z \hat{N}(A^I(Z_i,T)+k_1/2)[A^I(Z_i,T)+k_1/2] \\
k_3 &= \Delta Z \hat{N}(A^I(Z_i,T)+k_2/2)[A^I(Z_i,T)+k_2/2] \\
k_4 &= \Delta Z \hat{N}(\mathrm{e}^{\frac{\Delta Z}{2}\hat{D}}[A^I(Z_i,T)+k_3])\mathrm{e}^{\frac{\Delta Z}{2}\hat{D}}[A^I(Z_i,T)+k_3] \\
A(Z_i+\Delta Z,T) &= A(Z_i,T)+\mathrm{e}^{\frac{\Delta Z}{2}\hat{D}}[k_1+(k_2+k_3)/3]+k_4/6
\end{aligned} \tag{98}$$

This is the Fourth-Order Runge-Kutta in the Interaction Picture method, RK4IP.

4.1.5 The dispersion exponential

The dispersion exponential appears in several places in the RK4IP. For example, it acts on the normal amplitude when calculating the interaction amplitude

$$A^I(Z_i,T) = \mathrm{e}^{\frac{\Delta Z}{2}\hat{D}} A(Z_i,T) = \mathrm{e}^{-\frac{1}{2}\left(\alpha(\omega_0)+\sum_{l=1}^{\infty}\alpha_l \frac{i^l}{l!}\frac{\partial^l}{\partial T^l}\right)-\sum_{n=2}^{\infty}\beta_n \frac{i^{n-1}}{n!}\frac{\partial^n}{\partial T^n}} A(Z_i,T) \tag{99}$$

Using Fourier analysis, the derivatives in the exponential can be bypassed

$$\begin{aligned}
&\mathrm{e}^{-\frac{1}{2}\left(\alpha(\omega_0)+\sum_{l=1}^{\infty}\alpha_l \frac{i^l}{l!}\frac{\partial^l}{\partial T^l}\right)-\sum_{n=2}^{\infty}\beta_n \frac{i^{n-1}}{n!}\frac{\partial^n}{\partial T^n}} A(Z_i,T) = \\
&\mathscr{F}^{-1}\{\mathscr{F}\{\mathrm{e}^{-\frac{1}{2}\left(\alpha(\omega_0)+\sum_{l=1}^{\infty}\alpha_l \frac{i^l}{l!}\frac{\partial^l}{\partial T^l}\right)-\sum_{n=2}^{\infty}\beta_n \frac{i^{n-1}}{n!}\frac{\partial^n}{\partial T^n}} A(Z_i,T)\}\} = \\
&\mathscr{F}^{-1}\{\mathrm{e}^{-\frac{1}{2}\left(\alpha(\omega_0)+\sum_{l=1}^{\infty}\alpha_l \frac{i^{2l}\omega^l}{l!}\right)-\sum_{n=2}^{\infty}\beta_n \frac{i^{2n-1}}{n!}\omega^n} \mathcal{A}(Z_i,\omega)\}
\end{aligned} \tag{100}$$

where $\mathscr{F}$ denotes Fourier transformation. In this way the sums of derivatives are transformed to polynomials in frequency. Thus, the functions that the dispersion exponential are to operate on are Fourier transformed and multiplied by the frequency dispersion exponential, the products are then inversely transformed.

4.1.6 Occurring phenomena when using numerical Fourier transforms

The numerical model is set up in MATLAB, which uses a numerical algorithm to compute Fourier transforms called *fft*. This method computes the Fourier integral using numerical time steps of one. The transform must then be multiplied by the actual time step, used to set up the function to be transformed, if the energy is to be preserved and the spectrum is to show anything more than a relative distribution of the energy amongst the frequency components. The *fft* function will also give shifted spectra, such that the highest frequencies are centered in the middle, for real functions. They must therefore be shifted back using the function *fftshift*.

The Raman convolution is computed using the Fourier convolution theorem. As both the pulse power and the Raman functions are real valued, their convolution must also yield a real valued function. However, as the product of the Fourier transforms of the Raman function and the pulse power is inversely transformed, using the *ifft* function, it acquires small imaginary values. These values are a pure numerical artifact and will grow for each convolution they undergo. The solution is to take the absolute value of the inversely transformed product, using the *abs* function.

4.2 Solving the rate equations with an iterative fourth-order Runge-Kutta method

This section starts out with justifying why the rate equations, (82)-(85), can be solved in steady state and then outlines an iterative method to solve them.

4.2.1 Motivation for solving the rate equations in steady state

A propagating pulse will depopulate the excited electronic energy level due to induced stimulated emission. The amount of depopulation depends on the pulse's duration, form

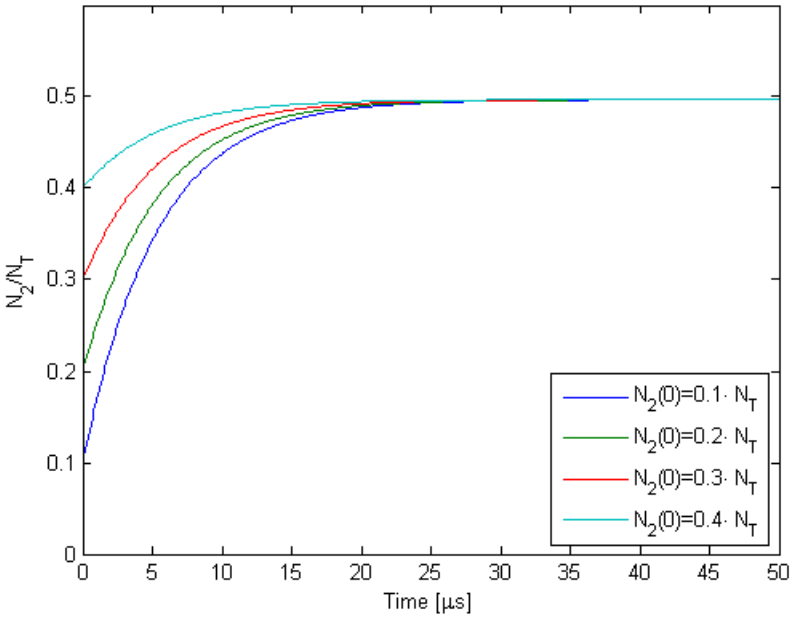

Figure 13: $N_2(t)$ at $z = 0$ for different initial conditions $N_2(0)$.

and energy. Depending on the pump's repopulation rate of the excited level and the pulses' repetition rate, the population of excited electrons can either be fluctuating with time or attain a non changing steady state profile.

The rate equations can be used to obtain the rate of the re-population along the fiber. However, due to fiber losses and absorption, the pump power will always be highest at the fiber end at which it is launched into. Therefore, analyzing the re-population at this end will give an upper limit to its rate.

Considering monochromatic continuous-wave pumping, the pump power will be constant at the end it is launched into and equation (82) is reduced to

$$\frac{\partial N_2}{\partial t} = \frac{\Gamma_p}{hcA_c}\lambda^p[\sigma_a(\lambda^p)N_T - (\sigma_a(\lambda^p) + \sigma_e(\lambda^p))N_2]P_p(\lambda^p) - \frac{N_2}{\tau} \tag{101}$$

where (83) was used. This equation can be solved analytically using the integrating factor, yielding

$$N_2(t) = \frac{\Gamma_p\lambda^p\sigma_a(\lambda^p)N_T P_p(\lambda^p)\left(1 - \mathrm{e}^{-\left[(\sigma_a(\lambda^p)+\sigma_e(\lambda^p))P_p(\lambda^p)+\frac{1}{\tau}\right]t}\right)}{hc\left((\sigma_a(\lambda^p) + \sigma_e(\lambda^p))P_p(\lambda^p) + \frac{1}{\tau}\right)} + N_2(0)\mathrm{e}^{-\left[(\sigma_a(\lambda^p)+\sigma_e(\lambda^p))P_p(\lambda^p)+\frac{1}{\tau}\right]t} \tag{102}$$

The parameters for the pump and active fiber that are to be simulated in this master thesis are given in Table 1, found in section 5. In Figure 13, (102) is plotted for different starting values of $N_2(0)$ for the extreme case of a pump power of 1000 W. Although this pump power is about two orders of magnitude greater than what is attainable from the laser diode that is to be used for pumping, the recovery time of N_2 is in the order of μs. Given that the pulses that are to be amplified have a repetition rate of 217 MHz, corresponding to 4.6 ns between consecutive pulses, the re-population rate will be insufficient to recover the upper level population along the fiber in between the pulses. This implies that the stimulated emission induced by the pulses and the pump will reach a steady state, where they balance each other.

Solving the rate equations in steady state will only include the effect of gain saturation on the total gain but not on the pulse shape, as that is a transient effect.

4.2.2 Solving the rate equations in steady state

The steady state settles in as the transient behaviors have vanished, which mathematically is expressed as the time derivatives in the rate equations, (82)-(85), being zero. Using (83) in (82) and solving for N_2 yields

$$N_2 = \frac{\frac{\Gamma_p}{hcA_c}\sum_{j=1}^{J}\lambda_j^p\sigma_a(\lambda_j^p)N_T P_p(\lambda_j^p) + \frac{\Gamma_s}{hcA_c}\sum_{k=1}^{K}\lambda_k^s\sigma_a(\lambda_k^s)N_T P_s^{\pm}(\lambda_k^s)}{\frac{\Gamma_p}{hcA_c}\sum_{j=1}^{J}\lambda_j^p[\sigma_a(\lambda_j^p) + \sigma_e(\lambda_j^p)]P_p(\lambda_j^p) + \frac{\Gamma_s}{hcA_c}\sum_{k=1}^{K}\lambda_k^s[\sigma_a(\lambda_k^s) + \sigma_e(\lambda_k^s)N_2]P_s^{\pm}(\lambda_k^s) - \frac{1}{\tau}} \tag{103}$$

which along with (84) and (85); that in steady state only contain z-derivatives, which means that they can be solved by the RK4 outlined in 4.1.3; gives the population density of excited electrons along the fiber.

4.2.3 Frequency decomposition of the signal

As the rate equations, (82)-(85), are wavelength dependent, the laser pulse is Fourier transformed to obtain its frequency constituents. The resulting spectrum is then renormalized such that its sum corresponds to the mean power. This is done by dividing the spectrum by its summation and multiplying the result by the mean power to be simulated. Since the Fourier transform by default is centered around the frequency zero, it is shifted such that the power spectrum instead is centered at the carrier frequency of the pulse, $f_0 = \frac{c}{\lambda_0}$. The frequency components of the power spectrum are then related to their corresponding wavelength through $\lambda = \frac{c}{f}$. Each wavelength constituent is then given its own propagation equation, (85). These propagation equations are coupled through the upper level population equation (103).

4.2.4 Co-propagating signal and pump

The situation when the signal and pump are coupled in at the same fiber end is referred to as co-propagation. Solving the steady state rate equations in this case starts with calculating $N_2(z = 0)$ using the incident pump and signal in (103). The value of $N_2(z = 0)$ is then used to propagate the pump and signal to $z = dz$ using (84) and (85). These values are used to calculate $N_2(z = dz)$ which is used to further propagate the pump and signal. This process is iterated until $z = L$, where L is the length of the fiber, where the following boundary condition is applied:

$$P^-(z = L) = R_L P^+(z = L) \tag{104}$$

where R_L is the reflectivity of the fiber end at $z = L$ and P represents both pump and signal power. After updating the values of the back propagating pump and signal, $N_2(z = L)$ is recalculated and used to propagate the signal and pump from $z = L$ to $z = 0$ in a similar manner as described above. At $z = 0$, the following boundary condition is applied:

$$P^+(z = 0) = P^+_{\text{ref}}(z = 0) + R_0 P^-(z = 0) \tag{105}$$

where P^+_{ref} represents the pump and signal powers that are launched into the fiber end $z = 0$ and R_0 is the reflectivity of that fiber end. The updated forward propagating pump and signal powers are then used to obtain $N_2(z = 0)$, which is then used to propagate the pump and signal along the fiber in the same way as described above.

The process of calculating N_2 from $z = 0$ to $z = L$ and from $z = L$ to $z = 0$ is iterated until the sum of the signal, both forward and back propagating, at the fiber end $z = L$ has not changed, more than some predetermined tolerance, between the last two iterations.

In the very first iteration, only the pump at $z = 0$ is propagated from $z = 0$ to $z = L$ and only the pump and back propagating signal are considered during the propagation from $z = L$ to $z = 0$.

4.2.5 Counter-propagating signal and pump

When the pump and signal are coupled in at opposite fiber ends, the situation is referred to as counter-propagation. In this case, the steady state rate equations are solved in the same iterative manner as in the co-propagating case but with the following boundary

conditions

$$P_s^+(z=0) = P_{\text{s ref}}^+(z=0) + R_0 P_s^-(z=0) \tag{106}$$
$$P_p^+(z=0) = R_0 P_p^-(z=0) \tag{107}$$
$$P_s^-(z=L) = R_L P_s^+(z=L) \tag{108}$$
$$P_p^-(z=L) = P_{\text{p ref}}^-(z=L) + R_L P_p^+(z=L) \tag{109}$$

where P_s and P_p denote the signal and pump powers respectively and the ref subscripts refer to the launched powers.

The first iteration is now solved by applying the pump from $z = L$ while the backward propagating signal, still the one propagating from $z = L$ to $z = 0$, is set to zero and the forward propagating signal is ignored in the propagation to $z = 0$.

Just like in the co-propagating case, this process is iterated until the signal, both forward and back propagating, at $z = L$ has not changed, more than some predetermined tolerance, between the last two iterations. However, as the last iteration is the one from $z = 0$ to $z = L$, the pump power does not necessarily reach its initial value at $z = L$. Therefore, an outer loop, that updates the initial value of the pump power until the final value at $z = L$ matches the applied power, is added. For each iteration of the outer loop, the initial pump's value is updated by adding the following factor to it

$$\text{corr} = \text{sgn}(P_0 - P_i) \cdot 10^{\text{floor}(\log_{10}(P_0 - P_i))} \tag{110}$$

where sgn denotes the sign function, floor denotes rounding off to the nearest lower integer, P_0 is the applied pump power and P_i is the current pump power as a result from the last rate equations solution from $z = 0$ to $z = L$. The corr-factor thus adds or subtracts a one times the order of magnitude of the difference between the applied and calculated pump power. The outer loop is set to run until the calculated pump power matches the applied one within some predetermined tolerance.

4.3 Combining the two models

The steady state rate equations are first solved for a given wavelength interval around the pulse's carrier wavelength. The resulting upper level population, $N_2(z) = N_2(Z)$, is used to obtain the absorption along the fiber. Using the right hand side of (76) and (83) the absorption can be expressed as

$$\alpha(Z, \lambda) = -\Gamma_s \left[(\sigma_e(\lambda) + \sigma_a(\lambda)) N_2(Z) - \sigma_a(\lambda) N_T \right] + \eta \tag{111}$$

The value for the absorption at each Z-point along the fiber is used in the GNLS to propagate the pulse to the next Z-point.

A flowchart of the program is given in Figure 14.

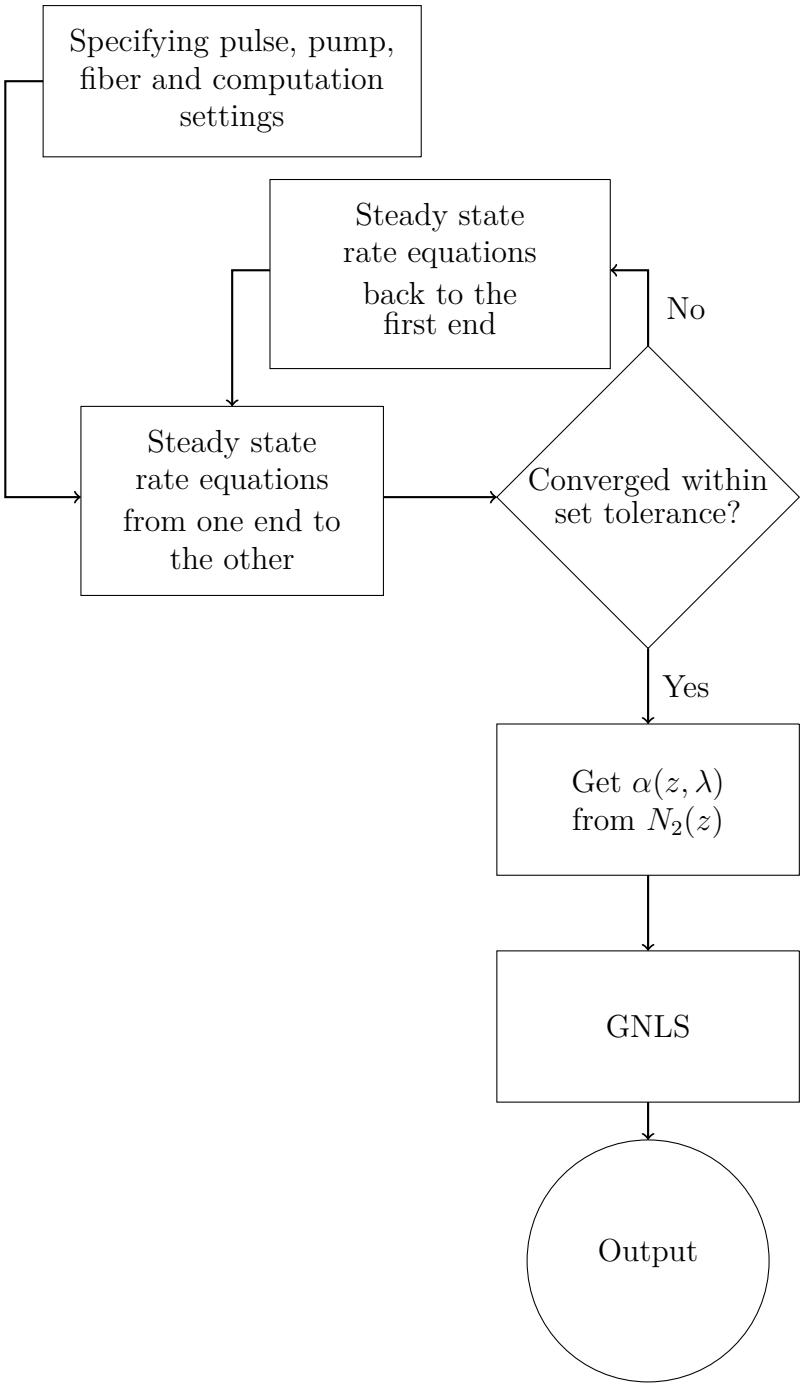

Figure 14: Flowchart of the program.

4.4 Numerically accounting for gain dispersion

As the cross section data used for solving the rate equations is experimentally collected, there is no analytic function for obtaining the expansion coefficients in (58). Therefore, the wavelength dependent absorption is instead polynomially approximated in the proximity of the carrier wavelength.

At each position along the fiber, the order of the polynomial approximation is chosen such that the absorption increases beyond the considered wavelength span. This is mainly done to avoid infinite values as a result of too large positive real numbers in the dispersion exponential, see (99), but also to ensure that the impact of the wavelength components in

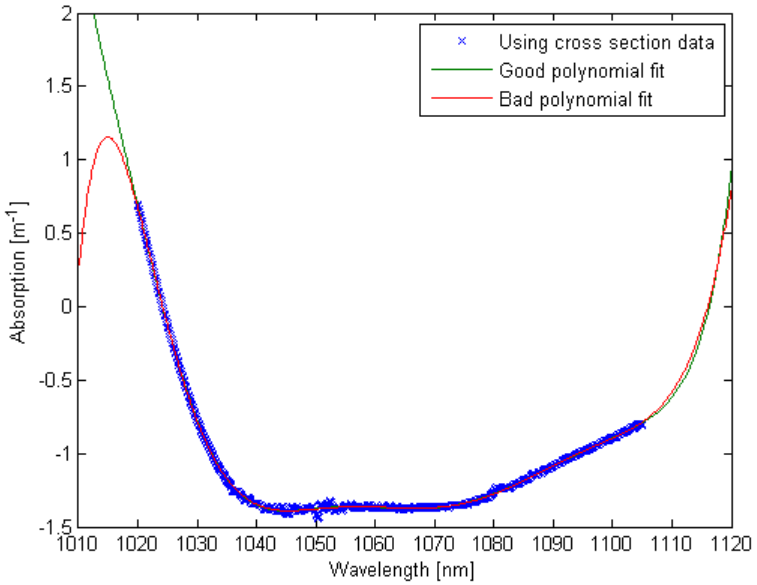

Figure 15: Choosing a suitable polynomial fit for the gain dispersion.

the considered wavelength span will be of most importance. Figure 15 shows the difference in absorption profiles when choosing a polynomial of order 10, the green graph, and 8, the red graph, to approximate the absorption, based on the cross section data, at a specific point along the fiber.

5 Setting the simulation parameters

In this section, the setting of the simulation parameters is detailed. These parameters are summarized in Table 1.

5.1 Parameters specifying the seed pulse

The pulse's full width half maximum, FWHM, was measured to be 170 fs and had a repetition rate of 217 MHz and a carrier wavelength of 1038 nm. The pulse amplitude had a transform limited, which means that the product of the pulse's time and spectral FWHMs is at its minimum and that the pulse is unchirped, hyperbolic secant time profile and a power envelope of a squared hyperbolic secant. The energy of such a pulse with a peak power of P_0 is obtained through the following integral

$$P_0 \int_{-\infty}^{\infty} \operatorname{sech}^2\left(\frac{T}{T_0}\right) dT = 2P_0T_0 \tag{112}$$

where $T_0 = \frac{\text{FWHM}}{1.7627}$. Multiplication with the repetition rate, R_r, yields the mean power.

$$P_m = 2P_0T_0R_r \tag{113}$$

Parameter group	Parameter	Value	Source
Seed	λ_0	1038 nm	Measured
	FWHM	170 fs	Measured
	R_r	217 MHz	Measured
	P_m	0.36 W	Measured
	Coupling efficiency	60%	Estimated
Pump	λ^p	976 nm	Measured
	Applied pump powers	$0.8 - 16$ W	Measured
	Coupling efficiency	85%	Estimated
Fiber	$\sigma_a(\lambda^p)$	$2.4254 \cdot 10^{-24}$ m^2	[1]
	N_T	$6.3 \cdot 10^{25}$ m^{-3}	Calculated
	τ	840 μs	[1]
	L	5.2 m	Measured
	r_{core}	10 μm	NUFERN specification
	r_{cladding}	200 μm	NUFERN specification
	η_s	-1 dBkm^{-1}	[16]
	η_p	-1.5 dBkm^{-1}	[16]
	γ	0.45 mW^{-1}m^{-1}	Calculated
	f_R	0.18	[9]
	τ_1	12.2 fs	[9]
	τ_2	32 fs	[9]
	Γ_s	0.97	Calculated
	Γ_p	0.0025	Calculated
	β_2	18 $\frac{ps^2}{km}$	Calculated
	β_3	0.042 $\frac{ps^3}{km}$	Calculated
	R_0	$8 \cdot 10^{-4}$	Calculated
	R_L	$8 \cdot 10^{-4}$	Calculated

Table 1: Summary of the simulation parameters.

Thus, the peak amplitude of the input pulse used in the simulations will be given by

$$A_0 = \sqrt{P_0} = \sqrt{\frac{P_m}{2T_0 R_r}} \tag{114}$$

for a given value of P_m. The seed input power simulated in this master thesis was 0.36 W. The amount of signal power that was actually coupled into the fiber was estimated to be 60%.

5.2 Parameters specifying the pump

The pump was a volume bragg grating stabilized continuous wave laser diode, LIMO40-F200-DL976-LM, operating at a wavelength of 976 nm. The pump beam was coupled into a delivery fiber with a core radius of 200 μm, which had a numerical aperture of 0.22. It was estimated that 85% of the pump's output power, ranging from 0.8 W to 16 W, was coupled into the active fiber.

5.3 Parameters specifying the fiber

The single mode double clad polarization maintaining Yb-doped active fiber had a core radius of 10 μm and a cladding radius of 200 μm. The fiber loss at the signal wavelength

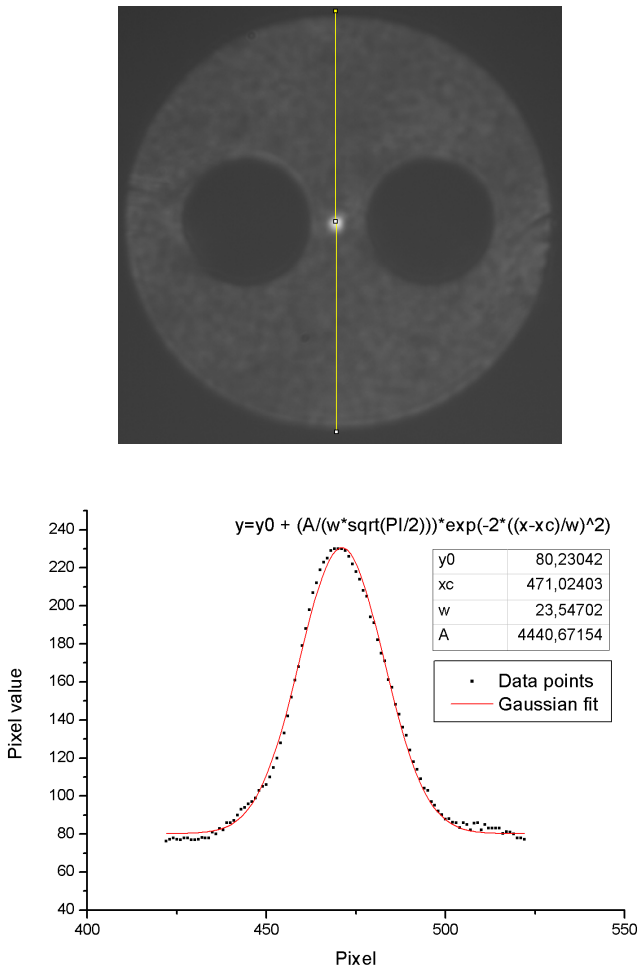

Figure 16: Line through the core and fitted Gaussian curve.

was set to -1 dBkm^{-1} and -1.5 dBkm^{-1} at the pump wavelength [16]. The upper level life time of the Yb-ions was 840 μs.

A fiber length of 5.2 meters was chosen as the fiber's small signal absorption at the pump wavelength, $\alpha_{ss} = 1.65\text{dBm}^{-1}$, suggests that almost 9 dB of the pump will have been absorbed by then. This implies that the pulse would not experience as much gain further on but instead just keep broadening due to longer interaction with the nonlinear effects.

The signal overlap factor, Γ_s, was approximated as the ratio between the core and effective mode area, giving a value of 0.97. The pump overlap factor Γ_p was approximated as the ratio between the core and cladding area, giving a value of 0.0025.

The amount of the pump that is absorbed per meter can be expressed as the product between the pump wavelength cross section, the pump's overlap factor and the doping concentration. Thus, the following differential equation can be set up

$$\frac{dP_{pump}}{dz} = -N_T \Gamma_p \sigma_{\text{abs}}(\lambda_{pump}) P_{pump} \tag{115}$$

This equation can be solved using the integrating factor, which gives

$$P_{pump}(z) = P_{pump}(0) \text{e}^{-N_T \Gamma_p \sigma_{\text{abs}}(\lambda_{pump}) z} \tag{116}$$

The small signal absorption expressed in decibel is defined as

$$\alpha_{ss} = 10\log_{10}\left(\frac{P_{pump}(z)}{P_{pump}(0)}\right) \tag{117}$$

Using this in (116) and setting $z = 1$ m and solving for N_T gives

$$N_T = -\frac{\ln\left(10^{\frac{\alpha_{ss}}{10}}\right)}{\Gamma_p \sigma_{\text{abs}}(\lambda_{pump})} \tag{118}$$

The absorption cross section value at the pump wavelength was $2.4{\cdot}10^{-24}$ m^2, which gave a doping concentration of $6.3{\cdot}10^{25}$ m^{-3}.

The effective mode area used to compute the nonlinear parameter γ in the GNLS, (46), was experimentally determined by analyzing an image of the output fiber end when the signal was applied without any pump. A Gaussian curve was fitted to the pixel values of one row through the core, this corresponds to approximating the transverse mode distribution as Gaussian, see Figure 16. The fitted w-parameter was used as the mode radius, thus the effective mode area was given by πw^2. The w-parameter was given in pixels, and was converted to meters by measuring how many pixels that corresponded to the cladding diameter of 400 μm. This resulted in an effective mode radius of 10.13 μm. The value for $n_2(\omega_0)$ was set to $5.33{\cdot}10^{-23}$ m^{2}V^{-2} and was obtained from the value of $n_2^I = \frac{2n_2}{cn(\omega_0)\epsilon_0}$ for 1053 nm, the measured value closest to the carrier wavelength, in [17]. $n(\omega_0)$, obtained from (119), was 1.45 for the carrier wavelength. This gave a γ value of 0.45 $m\text{W}^{-1}\text{m}^{-1}$. The Raman parameters τ_1, τ_2 and f_R were respectively set to 12.2 fs, 32 fs and 0.18 [9]. By using the Sellmeier model for the wavelength dependence of the refractive index of fused silica [18]

$$n = \sqrt{1 + \frac{0.6961663\lambda^2}{\lambda^2 - 0.0684043^2} + \frac{0.4079426\lambda^2}{\lambda^2 - 0.1162414^2} + \frac{0.8974794\lambda^2}{\lambda^2 - 9.896161^2}} \tag{119}$$

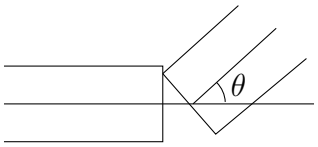

Figure 17: Two identical fibers with an angular offset of θ.

re-expressed as a function of $\omega = \frac{2\pi c}{\lambda}$, the group velocity dispersion expansion terms appearing in (59) were obtained by setting $k_L = \frac{2\pi\omega}{c} n(\omega)$ and using (51). In the final simulations, only the terms $\beta_2 = 18\ \frac{\text{ps}^2}{\text{km}}$ and $\beta_3 = 0.042\ \frac{\text{ps}^3}{\text{km}}$ were used. The fiber's end reflections can be approximated by analyzing the coupling of an optical signal between two identical fibers spliced with an angular offset, related to the fiber's cleave angle. Using the refractive index of the fiber's core at the carrier wavelength, n_c, the w-parameter of the optical signal, the angular offset between the fibers, θ, see Figure 17, and the wavelength, the amount of the signal that is coupled into the second fiber is given by [19]

$$T = \mathrm{e}^{-\frac{\pi^2 n_c^2 \theta^2 \mathrm{w}^2}{\lambda^2}} \tag{120}$$

By multiplying this amount with the Fresnel reflection at the cleaved fiber end, for a wave propagating parallel with the optical axis of the fiber, the reflected amount is obtained. As the cleaved end faces were perpendicular to the stress rods' axis that the polarization was aligned with, only the Fresnel equation for the s-polarization needs to be considered. Thus, the fiber's end reflections are given by

$$R = \left| \frac{n_c \cos\left(\frac{\pi}{2} - \theta_{\text{cleave}}\right) - n_t \sqrt{1 - \frac{n_c^2}{n_t^2} \sin^2\left(\frac{\pi}{2} - \theta_{\text{cleave}}\right)}}{n_c \cos\left(\frac{\pi}{2} - \theta_{\text{cleave}}\right) + n_t \sqrt{1 - \frac{n_c^2}{n_t^2} \sin^2\left(\frac{\pi}{2} - \theta_{\text{cleave}}\right)}} \right|^2 \mathrm{e}^{-\frac{\pi^2 n_c^2 \left(\frac{\pi}{2} - \theta_{\text{cleave}}\right)^2 \mathrm{w}^2}{\lambda^2}} \tag{121}$$

where n_t is the refractive index of the medium the signal is transmitted to from the core and the angle θ in Figure 17 was re-expressed in terms of the cleave angle defined in section 2.7.1, here denoted by θ_{cleave} instead of α as to not confuse it with the small signal absorption, α_{ss}. Using that the cleave angle was 85°, that the laser beam was transmitted

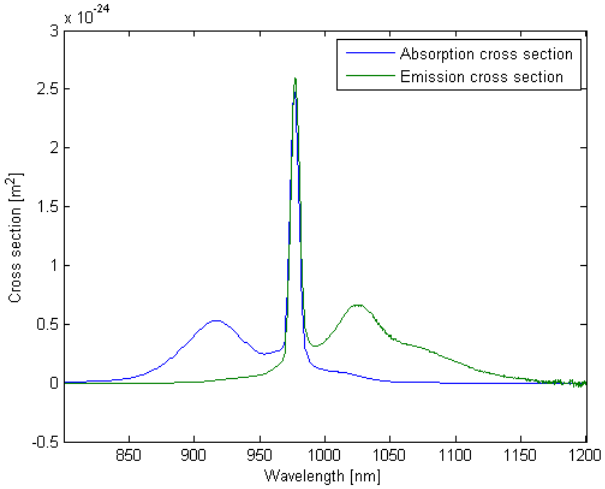

Figure 18: Experimentally collected cross section data from [1].

to air from the core, i.e. $n_t \approx 1$, the w-parameter and the refractive index for the carrier wavelength given above, the reflectance was found to be $8{\cdot}10^{-4}$.

The experimentally collected cross section data, obtained from [1], is shown in Figure 18.

5.4 Parameters specifying the computations

In this section, the parameters affecting the numerical computations are given.

5.4.1 Time steps

The MATLAB program was developed using test pulses with durations of a few ps to 100 fs. In order to resolve the time profiles of the short pulses, the sampling frequency must be high. To get a good resolved frequency profile, a wide enough time window of the pulses must be used. These parameters affect the number of data points and will thus determine the simulation time. Empirical optimization of these parameters lead to the following rules

$$\begin{aligned} \exp_{\text{ref}} &= \text{round}(\log_{10}(T_0)) \\ T_s &= 10^{\exp_{\text{ref}}-2} \\ |T| &\leq 5 \cdot 10^{\exp_{\text{ref}}-1.5} \end{aligned} \tag{122}$$

where $\exp_{\text{ref}}$ is a reference value, T_0 is the pulse duration, T_s is the time resolution, i.e. the inverse sampling frequency, and round denotes rounding off to the nearest integer.

5.4.2 Fiber steps, convergence limits and wavelength span

The fiber length of 5.2 m was discretized to 100 points. This fiber step was chosen as to not get too time consuming simulations. The RK4IP has a global error proportional to the fourth power of the fiber step, which in this case is only about $7 \cdot 10^{-6}$.

The convergence limit for the rate equations was set to 10^{-7} while the convergence limit for the counter propagating outer loop was set to 10^{-5}. These values were set such that they would not yield too time consuming simulations while still providing low risk of divergent numerical solutions.

The wavelength span ranged from 1020 nm to 1105 nm. This range was chosen as to cover a broad spectrum extending further towards longer wavelengths as to reflect the gain asymmetry of Yb, see Figure 18.

6 Experimental setup

To check the validity of the numerical model, a counter propagating cladding pumped laser amplifier, with a 5.2 m long Yb-doped fiber as amplifying medium, was set up. The fiber was pumped by a 976 nm laser diode. The pump beam was first collimated with a 40 mm lens. The collimated beam was then focused into the fiber through another 40 mm lens. The unabsorbed pump was then collimated through a 30 mm lens. The collimated unabsorbed pump was monitored to optimize the pump coupling into the fiber. The optimization was performed using a low pump power and adjusting the fiber position to maximize the ASE, which was read off a powermeter.

The mode-locked seed laser with 170 fs transform limited hyperbolic secant pulses at 1038 nm was then coupled into the fiber after passing a $\frac{\lambda}{2}$-plate, which was used to align the seed laser's polarization with the stress rods. The in-coupling of the seed was done using two mirrors, which were high reflective, HR, at 1038 nm and high transmitting, HT, at 976 nm, and two apertures. The mirror closest to the seed laser was adjusted such that the laser hit the middle of an aperture placed in front of the second HR mirror. The second mirror was adjusted such that the laser hit the middle of an aperture placed in front of the 30 mm lens. A third mirror with the same HR/HT characteristics as the other two mirrors was then inserted between the two 40 mm lenses, as to redirect the output signal away from the pump's path. A CCD-camera was placed in the beam path after the third mirror to facilitate the alignment. The fiber end facing the 40 mm lens was then de-collimated in order to image the fiber end onto the camera. The position of the fiber end closest to the seed laser was then adjusted to maximize the amount of saturated pixels in the core of the imaged fiber end. Once that was maximized, a powermeter was used to minimize the seed signal, as that suggests that the seed is absorbed in the core instead of guided through the cladding.

The fiber end facing the 40 mm lens was then collimated again and a glass plate was inserted in the path of the output beam path to couple the Fresnel reflection into a spectrometer. A powermeter was then placed in the transmitted beam path instead of the CCD-camera. Three metallic flip mirrors and two stationary metallic mirrors were inserted to give the possibility of coupling both the input and output beam into an autocorrelator for pulse duration measurements. Lastly, a powermeter was placed behind the second mirror that the seed laser passes so that the unabsorbed pump could be measured. The resulting setup is schematically illustrated in Figure 19.

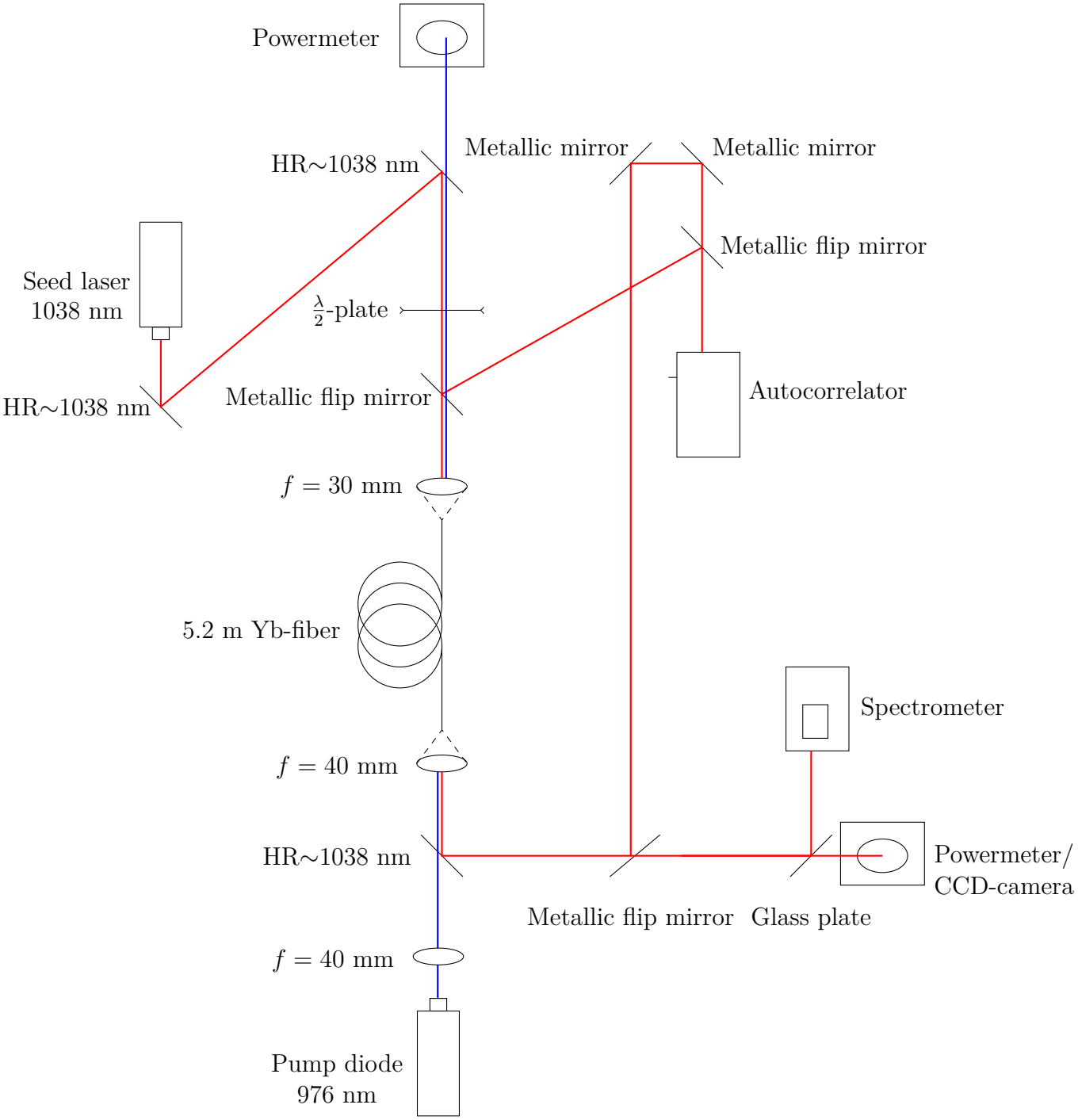

Figure 19: Experimental setup.

7 Results

Below, the results from the experimental setup and the simulations are first displayed separately and then compared to each other.

7.1 Experimental results

The experimentally collected amplifier characteristics from the setup in Figure 19 are given in Figure 20. Since the output power was measured after passing through a thick piece of glass, giving two Fresnel reflections, the measured value will be approximately 10% less than the actual output power. Taking this into account and subtracting the unabsorbed pump power, the slope efficiency of the laser amplifier, i.e. the slope of the output versus absorbed pump power, is 76 %.

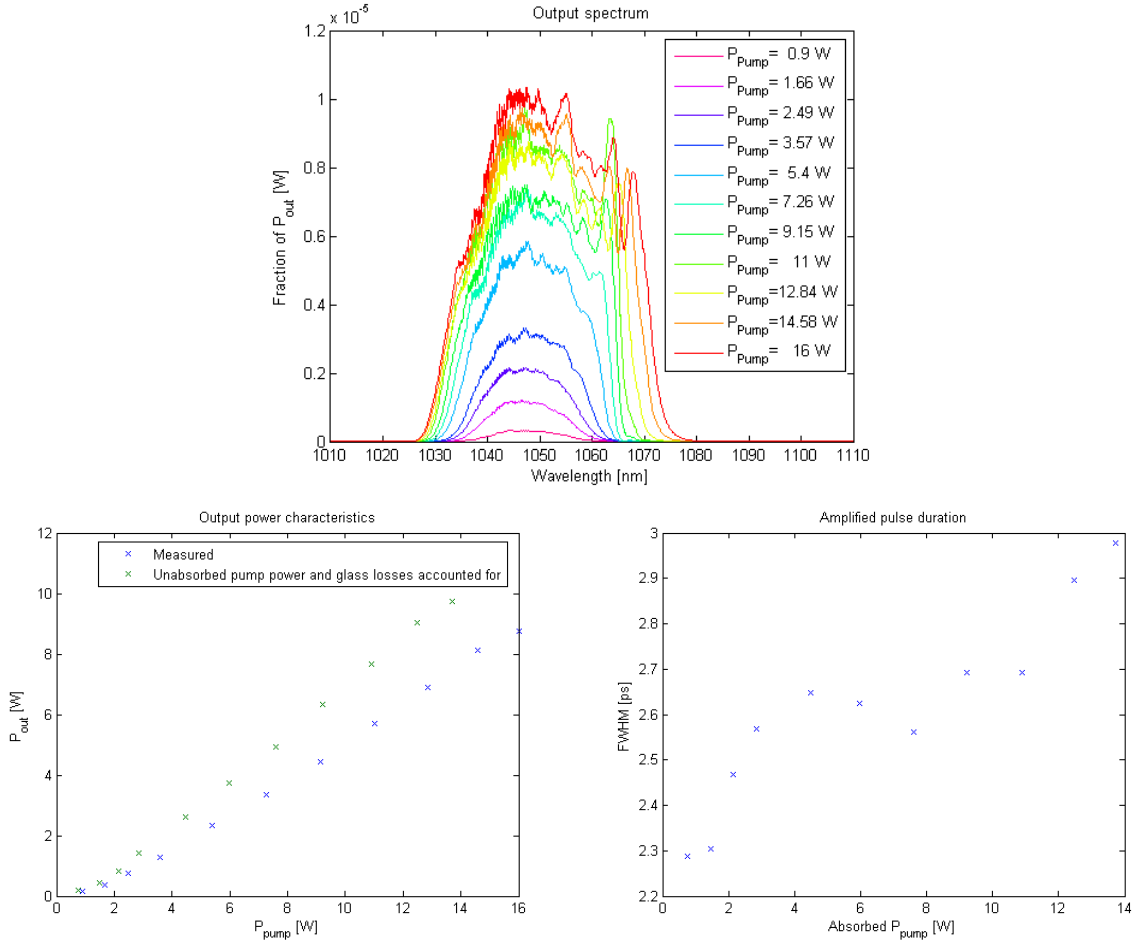

Figure 20: Measured spectrum, output power and FWHM of the output pulses for increased pump power.

7.2 Simulated results

The simulated results for the output power characteristics, inversion and pump profiles, time and spectral profiles, autocorrelation profiles and pulse durations, represented by the pulses' FWHMs, the relative change in powers and FWHMs between simulated points along the fiber are given in Figure 21. Rather than displaying the spectral intensity for the output spectrum, the power spectrum obtained by multiplying the absolute squared Fourier transform by the squared repetition rate is shown, this is done for easier com-

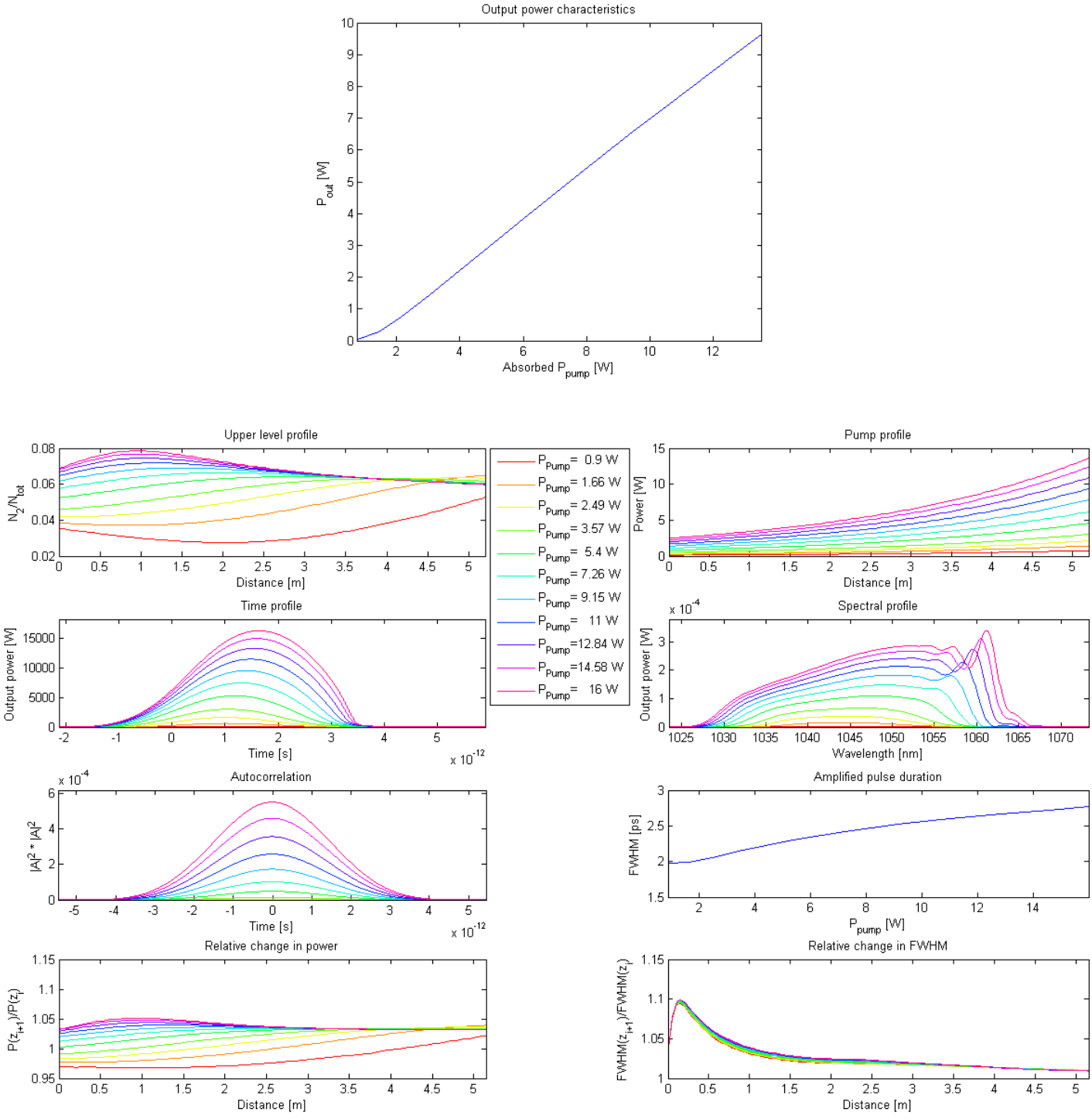

Figure 21: Simulated laser amplifier characteristics for multiple pump powers.

parison with the experimental data. The simulated pulse powers are calculated as the integrals, using a trapezoidal scheme, of the squared amplitudes multiplied by the repetition frequency. These powers correspond to the mean powers that would be read off a powermeter. Also, note that the simulated unabsorbed pump powers have been subtracted from the simulated launched pump powers in the top graph. This gives a simulated slope efficiency of 77%.

7.3 Comparison of results

The simulated and measured pulse durations, output powers and four of the output spectra are plotted together in Figure 22 for comparison. The measured output powers in this figure are those for which glass losses and unabsorbed pump power have been accounted for. For easier comparison, the spectra have been normalized by their peak value.

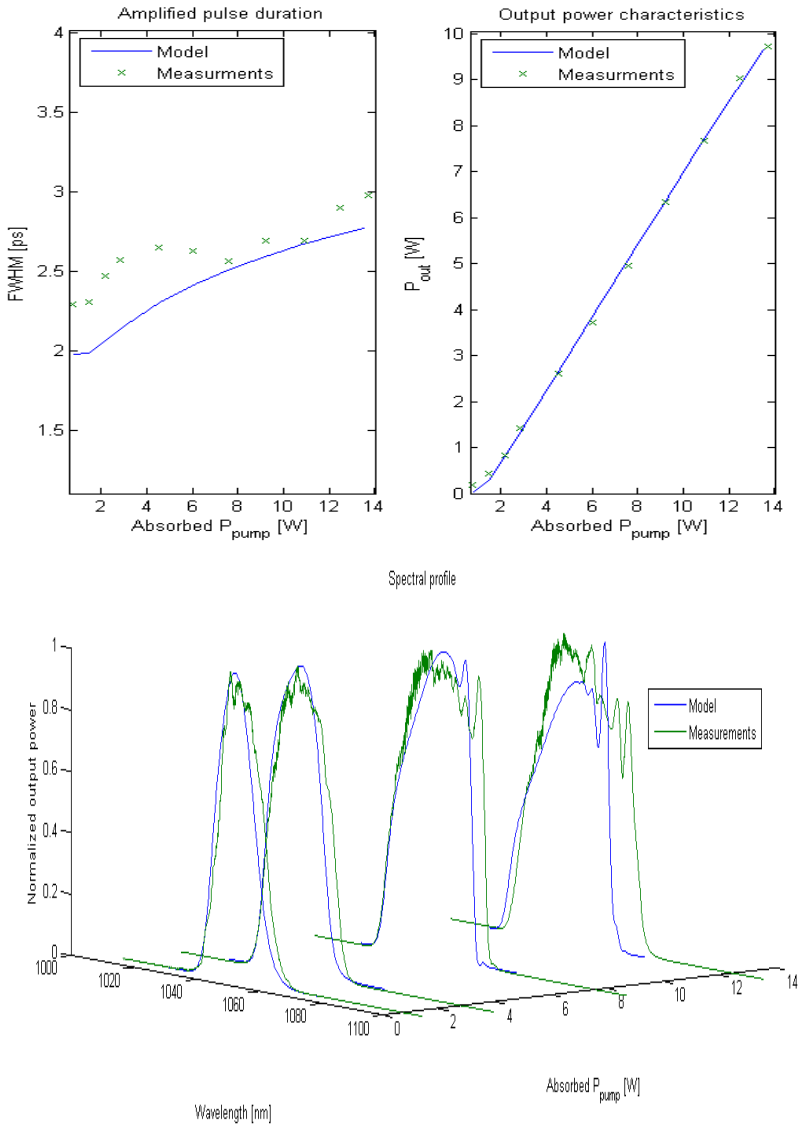

Figure 22: Comparison of simulated and measured amplifier characteristics.

8 Discussion

Figure 22 shows that the simulated output powers are in almost perfect agreement with the measurements, which suggests that the model is successful in modeling the pulse amplification as far as power gain is concerned.

The simulated pulse durations are all slightly shorter than the measured values. However, the curve formed by the simulated pulse durations closely resembles an average curve, with a vertical offset, that could be fitted in the middle of the measured values. This offset could be a consequence of:

- The GVD parameters being inaccurate and thus not broadening the pulse enough.
- The nonlinear parameter being too small to give enough spectral broadening through SPM. This would result in there not being enough new frequencies generated as the pulse propagates for the GVD to act on, which would cause the pulses to not broaden as much.
- Additional effects have to be taken into account, for example the neglected effect of gain saturation on the pulse shape might affect the pulse durations.

In Figure 22, it is seen that the measured and simulated spectra qualitatively show the same trend, i.e. being broadened more towards longer wavelengths and having ripples in the long wavelength part of the spectra at higher pump powers. However, quantitatively it is evident that the numerical model is incapable of broadening the spectra enough as the pump power is increased. This might be caused by:

- The Raman parameters not being accurate enough and thus not shifting the correct amount of energy to longer wavelengths.
- The nonlinear parameter being inaccurate and not yielding enough spectral broadening through SPM.
- The cross section data is invalid and does not yield enough gain for the longer wavelengths.
- Additional effects have to be taken into account, for example the neglected effect of gain saturation on the pulse shape might contribute in such a way that the spectra would be affected.

Due to the glass plate, only some percentage of the pulse will be coupled into the spectrometer. This means that the actual power spectrum should be about one order of magnitude greater than the measured one. Comparing the orders of magnitude for the simulated and measured power spectrum, indeed shows that the simulated spectrum is about one order of magnitude greater. The power spectra obtained from the steady state rate equations, see Figure 23, are about four orders of magnitude greater than the measured spectra and also have completely different shapes. This shows that they are insufficient for modeling pulse propagation.

Using the values for P_m, the signal coupling efficiency, γ, FWHM and β_2 in Table 1 in section 5 and (114) as well as (72) gives a $N \approx 1.1$, suggesting that neither the effects of SPM and GVD should be dominating. However, looking at the increase in spectral width in the measured spectra as well the increase in pulse duration as the pump power

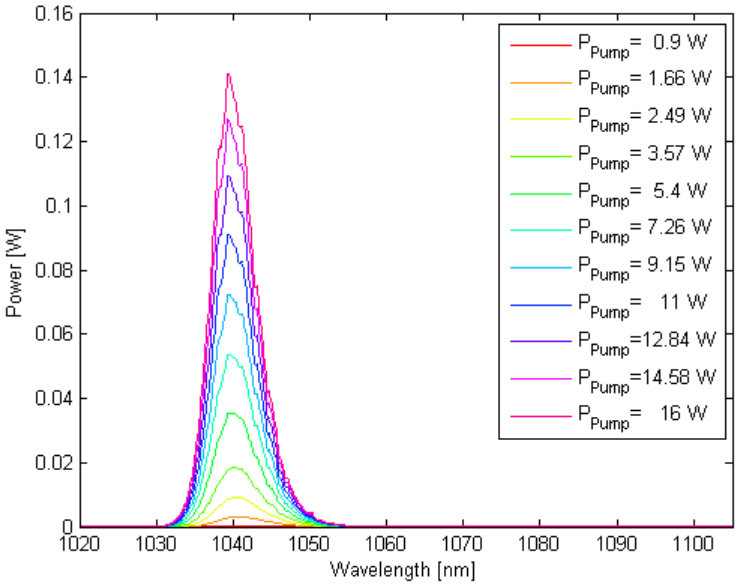

Figure 23: Simulated output spectra from the rate equations.

is increased, it seems like the spectral width increases more rapidly. To confirm this, the spectral width and pulse durations, normalized by the spectral width and pulse duration at the lowest applied pump power, were plotted. The result is shown in Figure 24, where it is also seen that the simulations show the same tendency. However, the relative increase in spectral width deviates more from the measured one as the pump is increased. This also suggests that either the simulation parameters are not in complete agreement with the actual setup and/or that more effects need to be considered.

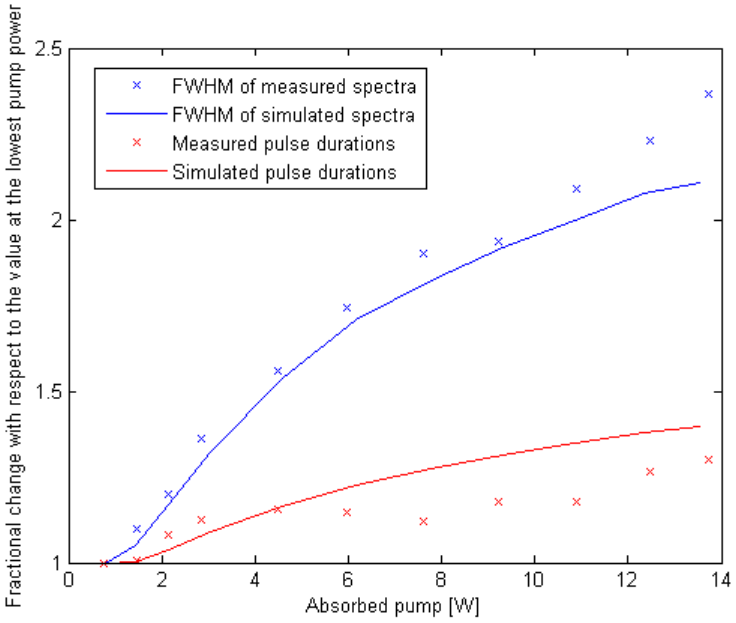

Figure 24: Relative increase in spectral width and pulse durations.

8.1 The relative importance of the GNLS terms

In order to investigate the relative importance of the different terms appearing in the GNLS, they are neglected in turns. The results are compared with the measurements in Figure 25. The measured output powers are the ones for which the glass losses and unabsorbed pump are accounted.

It can be seen that the simulated spectra are wavelength shifted compared to the measured ones when gain dispersion is neglected, see Figure 25a. This is a result of the spectra also being broadened towards shorter wavelengths. In turn, this means that there will be a greater variety of wavelength components propagating at different velocities because of the GVD. Therefore, the pulse durations are expected to increase more as the pump power is increased, which can be seen in the same figure.

Neglecting self-steepening and the Raman effect, see Figure 25b-c, does not affect the results by any noticeable amount.

However, also neglecting SPM has a tremendous impact, see Figure 25d. In this case, the only effect directly affecting the spectra is gain dispersion. This results in less pulse broadening through GVD as the pulse propagates, since there are no new wavelength components added to the spectra when the pulse is propagating. It also seems like the GVD and the gain dispersion start balancing each other as the pump power is increased. This can be seen by noticing that the spectra, which are actually being compressed as the pump power is increased, and the pulse durations, which are also compressed as the spectra are compressed, seem to change less as the pump power is increased.

The case when the Raman effect, self-steepening and the GVD are neglected does not yield pulse like solutions and are therefore not included.

This successive negligence of terms suggests that the most important effects to consider when solving the GNLS, for this amplifier configuration, are GVD, SPM and gain dispersion. It also implies that the impact of gain dispersion; which is an often neglected effect when solving the GNLS see for example [9], [11] and [14]; is necessary to consider in order to avoid getting wavelength shifted simulated spectra compared to the measured spectra, to get a similar trend for the simulated pulse durations as for the measured ones and a comparable slope efficiency.

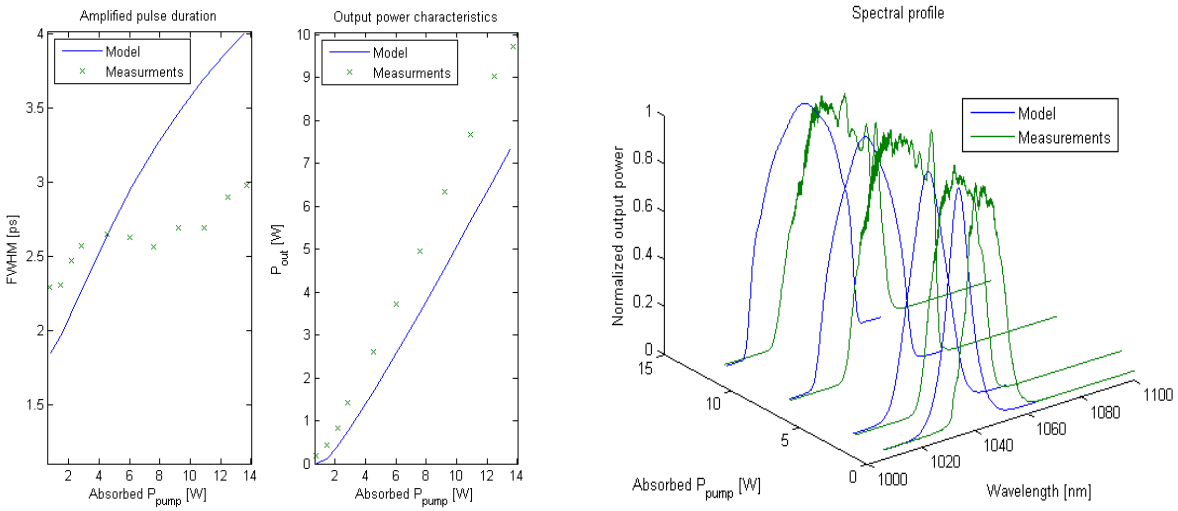

(a) Comparison of simulated and measured amplifier characteristics neglecting gain dispersion by only using the absorption for the carrier wavelength.

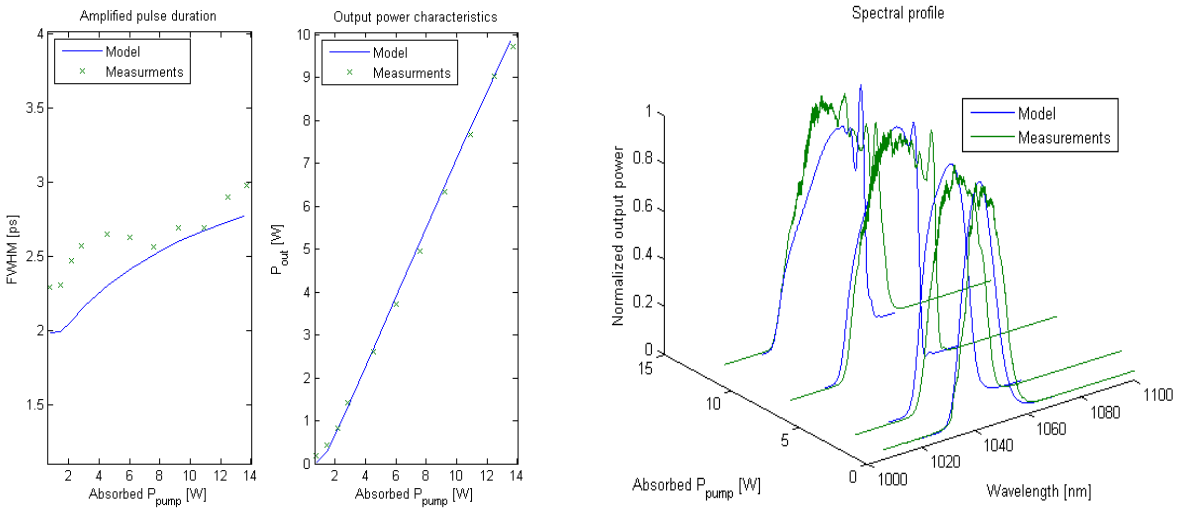

(b) Comparison of simulated and measured amplifier characteristics neglecting self steepening.

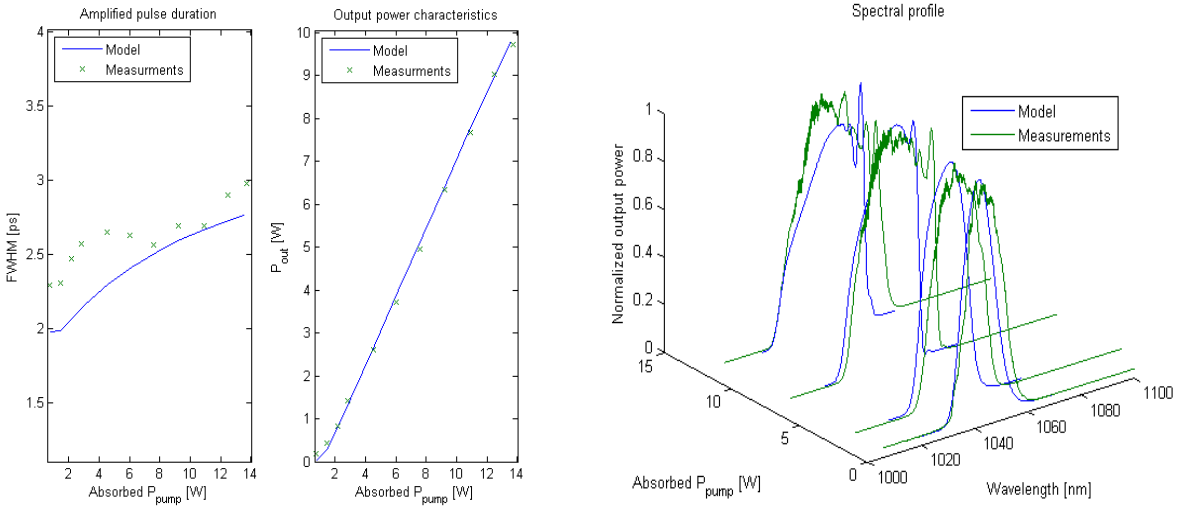

(c) Comparison of simulated and measured amplifier characteristics neglecting self steepening and the Raman effect.

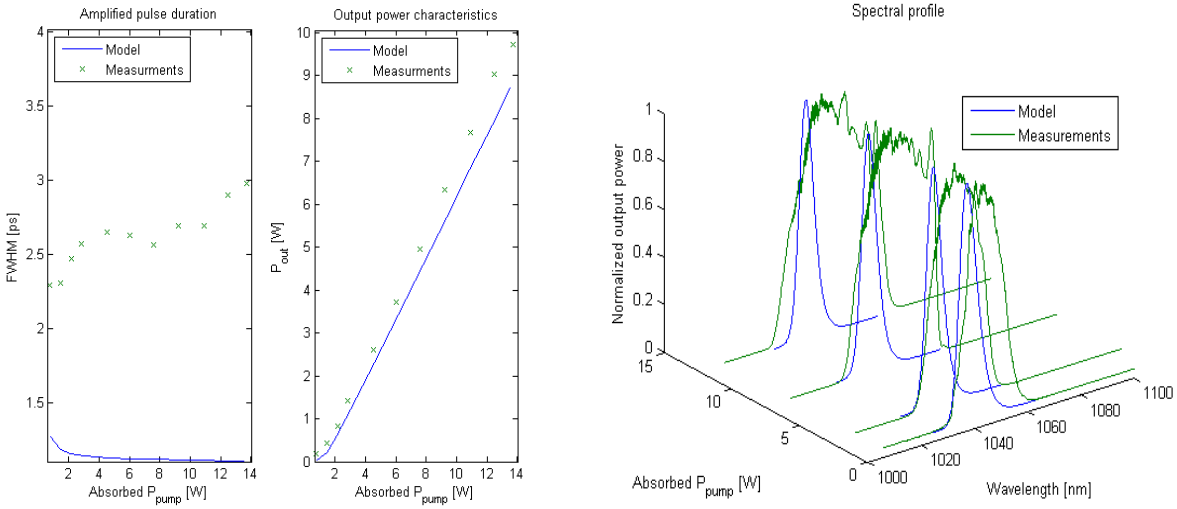

(d) Comparison of simulated and measured amplifier characteristics neglecting self steepening, the Raman effect and SPM.

Figure 25: The effects of neglecting terms in the GNLS.

8.2 The effect of a non uniform upper level population

To see the effect of accounting for the non uniform upper level population density; resulting from the varying absorption of the pump, stimulated and spontaneous emission along the fiber; the simulations are run using constant absorptions based on the measured data. These are obtained by

$$P(L) = P(0)\mathrm{e}^{-\alpha(\lambda_0)L} \Rightarrow \alpha(\lambda_0) = \ln\left[\left(\frac{P(0)}{P(L)}\right)^{1/L}\right] \tag{123}$$

where λ_0 denotes the carrier wavelength, $P(L)$ is the output power and $P(0)$ is the input power. The corresponding upper level populations are obtained by solving (111) for N_2 while using the cross sections for the carrier wavelength, giving

$$N_2 = \frac{\frac{\eta - \alpha(\lambda_0)}{\Gamma_s} + \sigma_a(\lambda_0)N_T}{\sigma_e(\lambda_0) + \sigma_a(\lambda_0)} \tag{124}$$

This value is then used in (111) to include the gain dispersion. The unabsorbed pump powers, subtracted from the launched pump powers to get the absorbed pump, are in this case the measured ones.

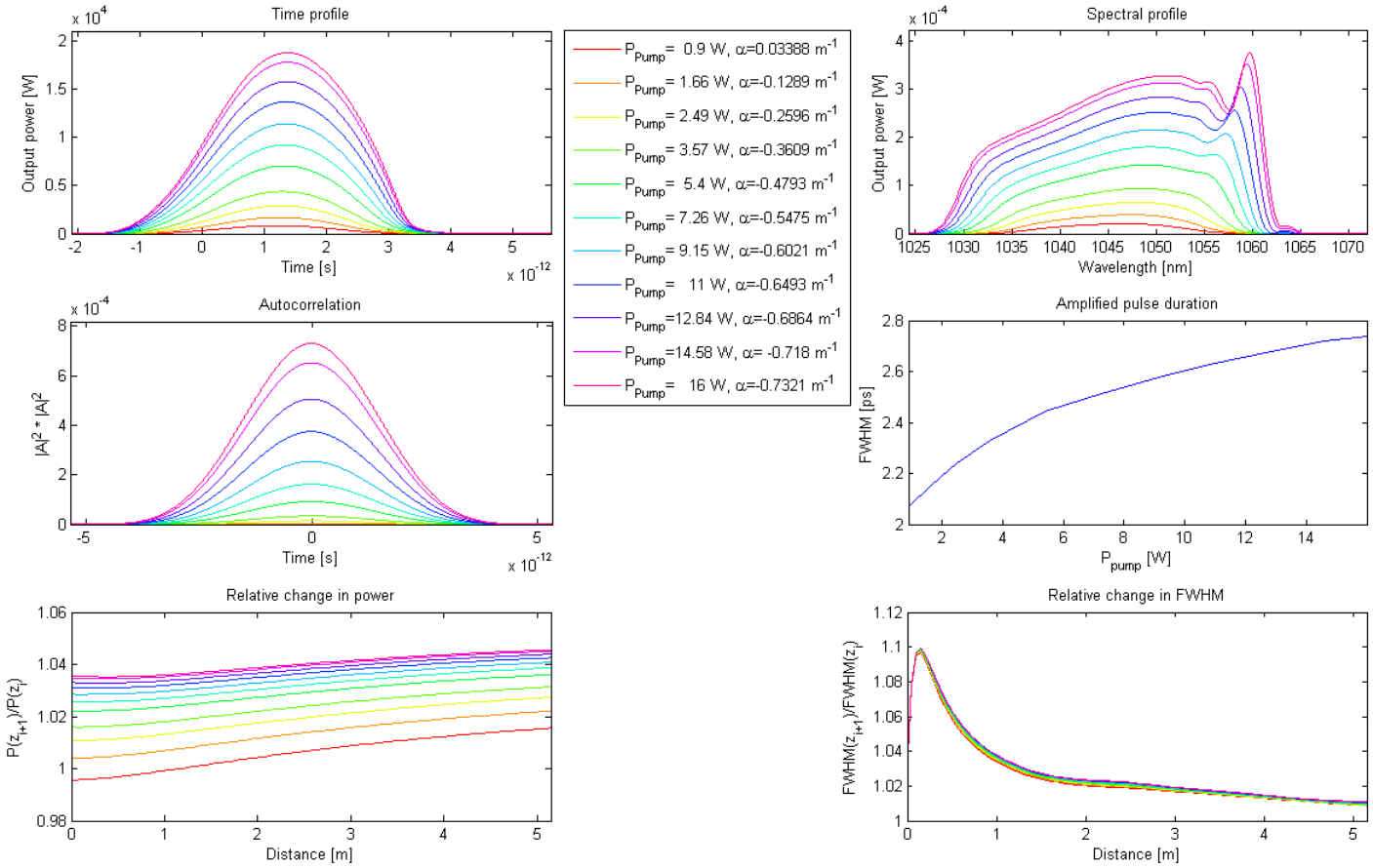

Figure 26: Simulated laser amplifier characteristics for increased pump power with constant absorption.

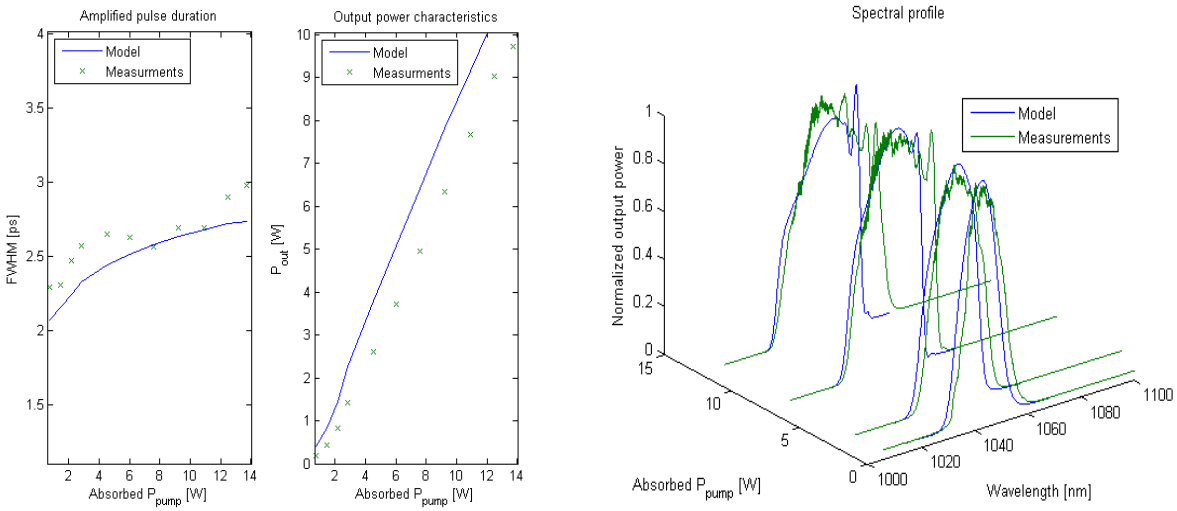

Figure 27: The effect of using constant absorption while solving the GNLS.

The simulated results are shown in Figure 26 and their comparison with the measurements are given in Figure 27. It is seen that the output powers are all greater than the measured ones, even at the lowest pump powers. However, the pulse durations and spectra give comparable results to the simulations where at least the non constant upper level population density, gain dispersion, GVD and SPM are accounted for.

Interestingly, these simulations give better correlation with the measurements than the ones neglecting gain dispersion but having a non constant upper level population. However, using this approach requires knowledge of the output power. It is therefore only possible to simulate already existing setups, unless the constant absorptions are estimated.

That these simulations correlate better with the measurements, than the simulations where gain dispersion was neglected, implies that only accounting for a nonuniform upper level population profile in the GNLS need not give better agreements with measurements than using a constant absorption.

It seems that the combination of a nonuniform upper level population and gain dispersion is required to give better agreement with measurements than just using a constant absorption.

8.3 The relative change in power and pulse duration

Looking at the simulated results in Figure 21, it is seen that the relative change in power very much follows the upper level profile, which was to be expected since the upper level population density determines the gain. It is evident; by comparing the relative power changes from the simulations with a constant gain, seen in Figure 26, to the ones in Figure 21; that after half of the fiber, the relative change in power in the case of a constant gain exceeds the one in the case with a non constant gain at all pump powers. This is the reason why the constant gains yield greater output powers.

In Figure 21, it can also be seen that the pulse is actually experiencing a net loss of power in the initial part of the fiber at the four lowest pump powers. At the two lowest pump powers, it takes more than half of the fiber before the pulses start experiencing a net gain. This could be an explanation as to why there seems to be a different gradient in the measured pulse durations between these two pump powers, see Figure 20. A comparison

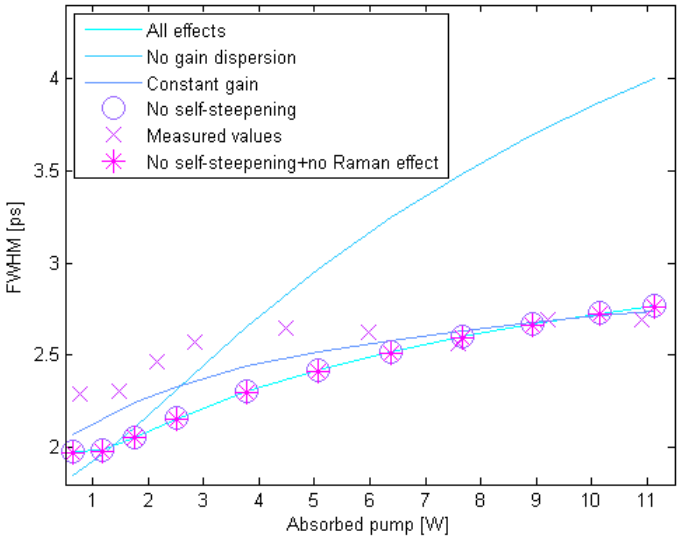

Figure 28: Comparison of the simulated pulse durations when neglecting different effects.

of the pulse durations in Figure 22, Figure 25a-c and Figure 27, is shown in Figure 28. In this figure, it is seen that a similar gradient between the two lowest pump powers, as the one in the measured pulse durations, is only present in the simulations where at least the non constant upper level population density, gain dispersion, GVD and SPM are taken into account.

Two interesting observations about the relative changes in FWHMs at different pump powers are that they follow very similar curves, even at the lowest pump powers unlike the relative changes in power, and that they mostly differ in the region 0.25-4 m. It is also interesting to note that the relative changes in FWHMs along the fiber are almost identical in Figure 21 and Figure 26. This and the discussion above suggest that as long as the pulse is experiencing a net gain throughout the entire fiber, the gain profile itself is not as vital for predicting pulse durations as it is for predicting pulse powers.

9 Conclusion and outlook

To conclude, a numerical model, combining the steady state rate equations with the generalized nonlinear Schrödinger equation, for simulating amplification of high repetition rate mode-locked laser pulses in active fibers was developed. The presented model accounted for effects such as GVD, SPM, self-steepening, the Raman effect, gain dispersion and non constant upper level population along the fiber.

A MOPA setup was set up to verify the model's validity by comparison of the simulated and the measured data. The results show that the simulated data is in very good agreement with the measured data in terms of output power characteristics, in good agreement in terms of pulse durations and in fairly good agreement in terms of output spectra.

Comparison of the simulations where effects were neglected in turns implies that gain dispersion on its own is a more important effect than a non constant upper level population density, whose importance was the main aim of this thesis to investigate, as far as correlation between the simulated and measured data is concerned. However, to asses whether this holds in general or only for the MOPA setup considered here, further measurements and simulations are required.

Although many of the simulation parameters used in this master thesis were tabulated values rather than measured values on the actual setup, the deviations between measured and simulated data are not that pronounced. Thus, as simulations often are used to understand general behavior, the presented model could be used for comparison between different fiber amplifier designs. However, further measurements should be carried out to assure the model's general validity before relying too much on such comparisons.

9.1 Future work

Below follows some potential future work for improving the presented model and for further testing its validity, as well as some possible future work for the experimental setup.

9.1.1 Implementing parallel computing

As the calculations for different simulated pump powers are independent, multiple pump powers could be simulated in parallel by implementing parallel computing. This would drastically reduce the simulation time when simulating more than one pump powers.

9.1.2 Improving the handling of gain dispersion

In principle, there could be several polynomial approximations that yield increased absorption outside the considered wavelength span. Thus, further restraint as to how the order of the polynomial approximation is chosen could improve the simulated results. Preferably some restraint which quantifies how well the polynomial approximation correlate with the absorption it is supposed to approximate. Another alternative would be to stitch several polynomial approximations together for different parts of the considered wavelength span.

The main problem however, is to acquire a valid behavior outside the considered wavelength interval.

9.1.3 Extending the model

As the presented model is based on the assumption that the transverse beam profile can be neglected, effects such as that the focused beams, pump and seed laser, are more intense in the center of the fiber are neglected. As the upper level population and all of the considered nonlinear effects are power dependent, the propagation conditions will depend on the radial distance from the center of the fiber. Thus, a transversely resolved model might be able to improve the simulated results.

It would be interesting to investigate whether an additional term could be included in the GNLS to account for the transient type of gain saturation, since that effect is neglected by solving the rate equations in steady state.

9.1.4 Further measurements

A continuation of this work should include measurements on a greater variety of pulses in terms of different input powers, durations, spectra and time profiles. These measurements should be compared to simulations using the presented model to provide a more general grasp of its validity.

Comparison of simulations and measurements on different fibers would also help in grasping the models' validity. Also, measuring the model parameters, see Table 1 in section 5, on the actual fiber, instead of using tabulated data, would yield a more fair comparison between the simulations and measurements.

9.1.5 Co-propagation

As the model only was tested for a counter-propagating amplifier setup in this thesis, it would be beneficial to investigate how well it works for co-propagating setups in order to get a better understanding of the models' validity.

9.1.6 Pulse compression

Since the pulses are broadened during the amplification, it would be interesting to experimentally investigate whether it is possible to compress them using for example a diffraction grating or a suitable optical fiber. It would also be interesting to see if the model presented here could be extended to include pulse compression as well.

9.1.7 Pumping nonlinear processes

Nonlinear processes, for example optical parametric oscillation where a photon gets converted into two photons of lower energy, require intense pump sources in order to have a good conversion efficiency. As the MOPA setup set up in this work was able to produce 3 ps pulses with a mean power of almost 10 W, it would be a good candidate for such a pump source.

References

[1] H. Pask, R. J. Carman, D. C. Hanna, A. C. Tropper, C. J. Mackechnie, P. R. Barber, and J. M. Dawes, "Ytterbium-doped silica fiber lasers: Versatile sources for the 1-1.2 pm region," *IEEE Journal of Selected Topics in Quantum Electronics*, vol. 1, no. 1, pp. B63–B92, 1995.

[2] D. Jochen, K. Alexander, M. Uwe, L. Alexander, L. Max, and K. Daniel, "Period doubling and deterministic chaos in continuously pumped regenerative amplifiers," *Optics Express*, vol. 12, no. 8, pp. 1759–1768, 2004.

[3] D. Richardson, J. Nilsson, and W. Clarkson, "High power fiber lasers: current status and future perspectives [invited]," *Journal of the Optical Society of America B*, vol. 27, no. 11, pp. B63–B92, 2010.

[4] J. Limpert, T. Schreiber, and A. Tünnermann, "Fiber-based high power laser systems," *Encyclopedia of Laser Physics and Technology*, 2013. http://www.rp-photonics.com/highpowerfiberlasers.html.

[5] C. R. Giles and E. Desurvire, "Fiber-based high power laser systems," *Journal of Lightwave Technology*, vol. 9, no. 2, pp. 271–283, 1991.

[6] C. Barnard, P. Myslinski, J. Chrostowski, and M. Kavehrad, "Analytical model for rare-earth-doped fiber amplifiers and lasers," *IEEE Journal of Quantum Electronics*, vol. 30, no. 8, pp. 1817–1830, 1994.

[7] J. R. Marciante and J. D. Zuegel, "High-gain, polarization-preserving, yb-doped fiber amplifier for low-duty-cycle pulse amplification," *IEEE Journal of Quantum Electronics*, vol. 45, no. 26, pp. 6798–6804, 2006.

[8] L. Hao, "Ytterbium-doped fiber amplifiers: Computer modeling of amplifier systems and a preliminary eletron microscopy study of single ytterbium atoms in doped optical fibers," 2011.

[9] G. P. Agrawal, *Nonlinear fiber optics*. Academic Press, 2007. Chapters: 1,2,3,4.

[10] E. Hecht, *optics*. Addison Wesley, 2002. Chapter 4.

[11] L. F. Mollenauer and J. P. Gordon, *Solitons in Optical Fibers: Fundamentals and Applications*. Elsevier Academic Press, 2006. Chapter 1.

[12] J. Marcerou, H. Fevrier, J.Ramos, J. Auge, and P.Bousselet, "General theoretical approach describing the complete behavior of the erbium-doped fiber amplifier," *Fiber Laser Sources and Amplifiers II*, vol. 1373, no. -, pp. 168–186, 1990.

[13] O. Svelto, *Principles of Lasers*. Academic Press, 2007. Chapters: 2.4.3,2.4.4.

[14] J. Hult, "A fourth-order runge-kutta in the interaction picture method for simulating supercontinuum generation in optical fibers," *Journal of Lightwave Technology*, vol. 25, no. 12, pp. 3770–3775, 2007.

[15] G. Eriksson, *NUMERISKA ALGORITMER med MATLAB*. KTH Datavetenskap och kommunikation, 2008. Chapter 8.

[16] J. M. Senior, *Optical Fiber Communications Principles and Practice*. Pearson Education, 2011. Chapter 3.3.1.

[17] D. Milam, "Review and assessment of measured values of the nonlinear refractive-index coefficient of fused silica," *Applied Optics*, vol. 37, no. 3, pp. 546–550, 1998.

[18] I. H. Malitson, "Interspecimen comparison of the refractive index of fused silica," *Journal of the Optical Society of America*, vol. 55, no. 10, pp. 1205–1208, 1965.

[19] D. Marcuse, "Loss analysis of single-mode fiber splices," *The Bell System Technical Journal*, vol. 56, no. 5, pp. 703–718, 1977.